Powder Technology 435 (2024) 119408

Contents lists available at ScienceDirect

Powder Technology

journal homepage: www.journals.elsevier.com/powder-technology

A numerical modeling framework for predicting the effects of operational parameters on particle size distribution in the gas atomization process for Nickel-Silicon alloys

Jinsong Hua [a,*], Federico Simone Gobber [b,*], Marco Actis Grande [b], Dag Mortensen [a], Jan Ove Odden [c]

[a] Dept. of Computational Materials Processing, Institute for Energy Technology, 2007 Kjeller, Norway
[b] Dept. of Applied Science and Technology, Polytechnic of Turin, 10129 Turin, Italy
[c] Elkem Silicon Products, 4675 Kristiansand, Norway

HIGHLIGHTS

- Propose a numerical modeling framework to simulate the gas atomization process.
- Consider the flow physics in both primary breakup and secondary breakup processes.
- Validate the numerical models with the results of gas atomization tests.
- Analyze the effects of atomizer operating parameters on particle size distribution.

GRAPHICAL ABSTRACT

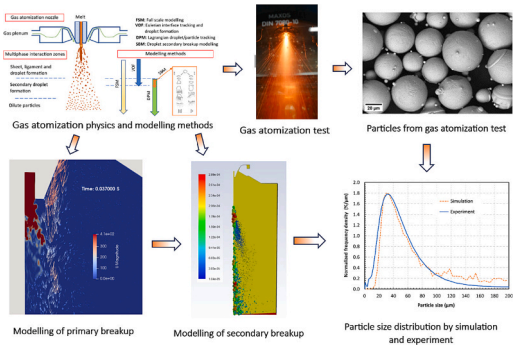

ARTICLE INFO

Keywords:
Gas atomization
Metal powder
Volume of fluid
Discrete phase model
Particle size distribution

ABSTRACT

Gas atomization is utilized to produce good-quality metal powders. A numerical modeling framework is developed to simulate the gas atomization process. A two-phase VOF flow model in OpenFOAM is applied to track the primary breakup of the melt stream by a high-speed gas flow. The generation of primary melt droplets is extracted from the VOF field. A Lagrangian-Eulerian multiphase flow model in Ansys Fluent is adopted to track the secondary breakup of the primary melt droplets under the high-speed gas flow. The final particle size distribution is obtained by analyzing the particles sampled at the outlet of the atomization chamber. The process of gas atomization can be affected by many factors such as the atomization equipment, operating parameters, and material properties. Sensitivity analysis is conducted through modeling to investigate the effects of these factors on particle size distribution. The model predictions are validated by specially designed gas-atomization experiments.

* Corresponding authors.
E-mail addresses: jinsong.hua@ife.no (J. Hua), federico.gobber@polito.it (F.S. Gobber), marco.actis@polito.it (M. Actis Grande), Dag.Mortensen@ife.no (D. Mortensen), jan-ove.odden@elkem.com (J.O. Odden).

https://doi.org/10.1016/j.powtec.2024.119408
Received 27 November 2023; Received in revised form 5 January 2024; Accepted 10 January 2024
Available online 11 January 2024

1. Introduction

Additive manufacturing (AM) has been transitioned successfully from a prototyping tool to an established and economical method for functional component production [1]. For the popular AM technologies such as Powder Bed Fusion and Direct Energy Deposition, metal powder characteristics [2,3] such as particle morphology, size distribution, flowability, and bulk density, play very important impacts on both the AM processes and the functional quality of the component produced. The matching of powder characteristics to any specific application (AM machine) and the requirements of product-specific function becomes crucial. Hence, to produce good quality powders for AM applications, the powder production process and its operating parameters should be optimized.

Some standard powder production techniques [3,4] have been developed to produce high-purity and quality metal powders. Among them, gas atomization of liquid metals is a very efficient process employed in the powder metallurgy industry, yielding very small and spherical powders compared to other conventional techniques [5]. The gas atomization process utilizes a high-speed cold inert gas stream to disintegrate a high-temperature metal melt stream, resulting in atomized metallic droplets, which rapidly solidify to form metal powders without significant segregation [6]. Due to the very high cooling rate experienced by the powders, excellent mechanical and chemical properties can be achieved. Such powders are also highly spherical which is important because good flow characteristics and dense packing are required for AM applications. The gas atomization process also enables great control of various powder properties [7–9] and thus shows potential for mass production [3,6]. Therefore, it is important to understand the effect of each operating parameter on the gas atomization process and the powder size distribution.

The gas atomization process involves the complex multiphase coupling between the high-speed gas jet and the high-temperature molten metal stream, which occurs under the conditions of extremely high momentum and energy exchanges through the liquid-gas interface disintegration. Gas atomization experiments have been conducted to understand the correlations between particle formation and the various atomization process parameters [8,10,11]. The process conditions such as physical properties of feed materials of both hot metal liquid and cold gas jet, atomization nozzle specification, operating parameters, and spray-tower geometry, determine the final properties of metal powders in terms of size distribution and morphology by influencing the breakup dynamics of the primary liquid sheet into small droplets and the cooling of droplets to fine particles in the spray chamber. To understand the interaction process between the melt stream and the high-speed gas jet, the breakup process of the liquid stream into droplets was studied using high-speed photography technology [10,12,13], and the gas flow field was investigated using the PIV technique [14] and schlieren technology [15,16]. It is difficult and costly to study the effects of detailed multiphase flow physics on particle formation through gas atomization experiments. To compensate for the limitations of experimental methods, numerical modeling provides another approach to investigate the flow physics involved in the gas atomization process. The experimental results under certain specific conditions are also useful in validating the numerical models.

The gas atomization process can be divided into two regimes: primary and secondary atomization. The primary atomization regime starts when the melt interacts with the high-speed gas flow. The melt stream will deform and create an unstable wave-like structure, and then it breaks up into ligaments and large droplets [7,17,18]. The secondary atomization regime begins further downstream when the large droplets and ligaments extend due to the interfacial instability and break up into smaller droplets [5,19–21]. This breakup process will continue until the critical Weber number is reached or till the droplet is solidified. In decades, various computational-fluid-dynamics based multiphase modeling algorithms and software tools [5–7,11,14,17,19,20] are developed to simulate the gas atomization process, building in-depth perception of the gas-melt interactive effect, disintegration of melt steam, and distribution of molten droplets and solidified particles within the atomization region. Tong and Browne [22] made the first try at simulating the interaction of the melt stream and gas jet in the gas atomization process using a two-phase flow modeling approach (front tracking method) in a 2D model. Even though their simulation did not show the formation of droplets and ligaments, it highlighted the importance of two-phase flow dynamics in the gas atomization process. Zeoli et al. [23] simulated the primary atomization process for different types of atomizers in 3D models using a volume of fluid (VOF) two-phase flow modeling method. Their simulations showed the gas-melt interaction at the early stage of primary atomization. Zhao et al. [24] simplified the geometry of the 3D gas atomizer into a 2D axisymmetric model to simulate the primary atomization process using the VOF method in Ansys Fluent. The simulation showed the melt stream was spread radially by the circulating gas under the melt nozzle and was stretched downward by the gas jet at the outside of the nozzle tip. However, the primary breakup of the melt stream into droplets was not observed in the simulation. Arachchilage et al. [7] studied the gas atomization process of aluminum at different gas atomization pressures in a 3D quarter-sector cylindrical model using the VOF method in OpenFOAM. The fragmentation of melt flow into droplets was simulated. The simulations predicted the effect of gas pressure on the droplet size distribution at the early stage of primary atomization. Compared to the particle size distribution of the powders obtained at the end of experiments, the predicted droplet size distributions had large discrepancies. This is because the secondary breakup of droplets is not included in the modeling. Wang et al. [11] simulated the gas atomization process of 316 L stainless steel at a three-dimensional scale. The formation of droplets via liquid-metal flow tearing and breaking by a close-coupled atomizer was simulated using the VOF multiphase flow in Ansys Fluent. Local mesh refinement was adopted to capture the primary atomized droplets. Small droplets were converted to drop particles and tracked using a Lagrange method. The secondary breakup of small droplets was considered in the modeling. The particle size distribution was obtained from the simulation and was in reasonable agreement with the experiments. The recent work of Wang et al. [25] applied a VOF model to investigate the primary atomization behavior of a twin-nozzle gas atomization process. The effect of various primary and secondary pressures on the gas flow field, melt atomization, particle characteristics (particle diameter, sphericity, and satellite particles), and phase structure were investigated through numerical simulations and experiments.

Some of the early numerical models [22,23], due to the limitation of computational resources, could not successfully predict the fragmentation of melt flow by the high-speed gas jets in the primary breakup process, and the number of droplets captured by the simulation was very limited. Hence, the Eulerian-Lagrangian approach [19–21] was also used to investigate the gas atomization of molten metal and particularly the secondary breakup process. The primary atomization was ignored, and the model inputs of initial droplet size and location were based on assumptions. Zeoli and Gu [21] focused on the cooling/solidification process of the in-flight droplets. The droplet breakup was also considered using the Taylor analogy (TAB) breakup model and Kelvin-Helmholtz (KH) instability model. Firmansyah et al. [26] included the two-way coupling between gas and the droplets with a focus on the droplet size distribution after the secondary breakup. Both the TAB and KH instability models were employed. The effect of initial droplet sizes on the final particle size distribution (PSD) was studied and verified by the experiments. Thompson et al. [19] concluded that the Kelvin-Helmholtz Rayleigh-Taylor (KHRT) breakup model could be utilized to predict the particle size distribution due to the secondary atomization. The model was employed to study the effect of operating parameters on the PSD in the gas atomization process. Recently Shi et al. [6] made good predictions on the particle size distribution after the secondary atomization using the WAVE model in Ansys Fluent.

In addition, a simulation approach with a combination of Volume of Fluid (VOF) and Discrete Phase Model (DPM) was proposed by Wei et al. [27] to analyze the gas atomization process. The VOF method was applied to simulation the primary breakup of the melt stream in a 2D axisymmetric model. The Large-Eddy Simulation (LES) model could more accurately capture the large droplet separation process from the liquid column than the SST k-ω model. The DPM model was applied the simulate the secondary breakup model. The injection of the primary droplets was based on the primary breakup simulation result of the VOF model. They had constant positions, velocities, sizes, and mass flow rates. A similar numerical method was applied by Luo et al. [28] to simulate the formation of powders and the evolution of the defects in the gas atomization process. The primary breakup process was simulated using the VOF method with a dynamic adaptive mesh. Three injections of primary droplets were defined from the primary atomization simulation. These injections were constant in the secondary breakup simulation. The recent work by Wang et al. [29] used a similar numerical approach to study the influence of the atomization pressure and melt mass flow rate on the melt breakup behavior and the powder size distribution. The size range of the primary droplets was obtained from the primary atomization simulation. An assumption of rosin-rammer size distribution was applied to initialize the particle injections in the DPM for the secondary breakup process modeling. Although the 2D axisymmetric models [27–29] require less computing resources and time to simulate the primary breakup process, they fundamentally can only predict the formation of "ring-shaped" droplets, not "sphere-shaped" droplets, resulting in errors in estimating primary droplet size, velocity, and position. Amatriain et al. [30] proposed another two-stage multiphase model for close-coupled gas atomization by combining an Eulerian multiphase model for the primary atomization and a Lagrangian particle tracking approach for the secondary atomization. A convection-diffusion equation for the liquid-gas surface density was solved and used to estimate the particle size. For the secondary atomization simulation, the injection of primary droplets with constant size at the estimated gas-liquid interface was assumed.

In this study, a CFD-based numerical modeling framework is proposed to simulate the gas atomization process of molten nickel silicon alloys with a focus on the model's capability to predict the final particle size distribution. Both the primary and secondary atomization processes are included in the modeling framework. The primary atomization process is simulated transiently using the VOF multiphase flow model of OpenFOAM within a small computational domain under the atomization nozzles with very fine mesh grids. Hence, the complex interaction between the melt stream and the annular high-speed gas jet can be captured. The disintegration of the melt stream and the formation of ligaments and droplets are revealed in the simulation. At the outlet boundary of the computational domain, the droplets tracked by the Eulerian VOF method are converted into discrete droplets, where the information on droplet size, velocity, position, and time are recorded dynamically. The secondary atomization process is simulated transiently using the Euler-Lagrangian Discrete Phase Model (DPM) of Ansys Fluent within a relatively large computational domain including the high-pressure gas chamber, gas expansion flow path, and atomization chamber. The continuous gas flow is obtained by a compressible gas flow model. The droplets of the discrete phase are injected into the model according to the droplet information recorded in the primary atomization simulation. The movement and cooling of the droplets are tracked in a Lagrangian manner. The secondary breakup of the droplets is modeled using the KHRT model. The particles reaching the outlet of the atomization chamber are sampled. The particle size distribution is obtained through statistical analysis of the sampled particles. The turbulence model of Large-Eddy Simulation (LES) is adopted for simulating high-speed gas flows. Gas atomization tests are designed and performed to verify the numerical model performance. The particle size distributions obtained from the simulations and experiments are compared, and they are in good agreement. In addition, the effects of different operating parameters and material properties on the final particle size distribution are studied. It shows that the gas atomization process is controllable to produce powders with good quality by regulating the operating parameters.

2. Numerical modeling framework

2.1. Flow physics in gas atomization process and modeling strategy

A schematic cross-section diagram of a typical gas atomization nozzle is shown in Fig. 1. High-pressure gas is supplied through the side opening nozzle to the gas plenum. Then, the high-pressure gas exhaust from the opening slit to the atomization chamber at a supersonic speed, with a focusing point under the melt delivery tube. Molten alloy flows from the crucible to the atomization chamber through the guide tube. The melt stream will be disintegrated by the high-speed gas under the gas atomization nozzle. The gas atomization process can be divided into several basic stages: primary melt steam breakup, secondary droplet breakup, solidified droplet, and dilute particle loading flow, which occurs in different multiphase interaction zones as shown in Fig. 1. At the primary breakup stage, the melt liquid core interacts with the cold gas jets near the nozzle tips. The melt stream will deform and create unstable wave-like structures, then it breaks up into ligaments and large droplets. At the secondary breakup stages, the primary large droplets and ligaments are stretched/dragged further by the high-speed gas flow. Due to the fast-growing Rayleigh-Plateau instability and Kelvin-Helmholtz (KH) instability, the primary droplets will break up into smaller droplets. This breakup process will continue until the critical Weber number is reached or till the droplet is solidified due to the cooling by the cold high-speed gas flow. Finally, the solidified particles will be cooled further by the gas flow inside the atomization chamber. Larger particles settle down at the bottom of the atomization chamber and are collected as powder products. Fine particles are extracted from the atomization chamber and collected through a side gas-particle separating cyclone.

The gas atomization process has been studied using various experimental approaches. However, due to the high complexity in the flow physics of multiple length scales, material phase states, and strong flow turbulence, it is still very challenging to understand the physics details and provide specific guidance to control the operational parameters to produce the particles with the required characteristics, e.g. particle size distribution. Physics-based CFD modeling provides another cost-effective approach to investigate the gas atomization process, which can greatly compensate for the limitation of the experimental approach. As shown in Fig. 1, the CFD-based modeling method can be classified into three categories: full-length scale modeling, Eulerian interface and phase volume fraction tracking, and Lagrangian discrete particle tracking. The full-length scale model (FSM) intends to resolve the dynamics of droplets and particles in all sizes through very fine mesh or adaptive mesh refining and coarsening methods. The accuracy of this type of numerical model depends strongly on the smallest length scale which can be resolved numerically. The model with a larger number of mesh grids has a high demand for computational resources and needs a longer simulation time, which makes it impractical for engineering process optimization. The Eulerian interface tracking method (e.g. VOF) is good at simulating the dynamic behavior of the melt-gas interface and the droplet formation during the primary breakup process. This method is good at simulating the primary droplets above a certain length scale (i.e. $> 100\ \mu m$). It could be very computationally costly to resolve droplets with small diameters (i.e. $10\ \mu m$). On the other hand, the Lagrangian particle tracking method (e.g. DPM) is good at modeling the secondary breakup of large droplets into fine droplets and the particle temperature variation. The simulation results depend upon the input conditions for particle injections such as droplet size, position, velocity, temperature, etc.

To combine the advantages of both the Eulerian Interface Tracking method and the Lagrangian Particle Tracking method, a new modeling

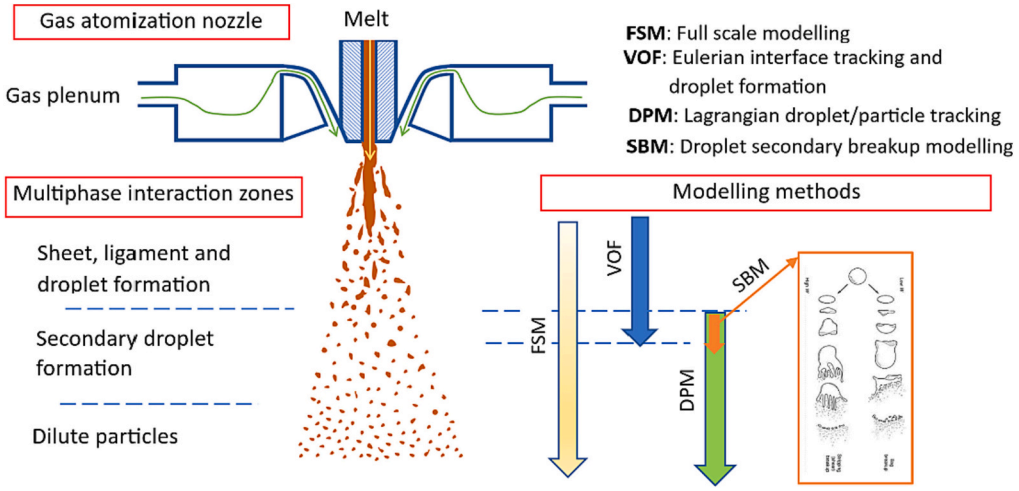

Fig. 1. Gas atomization physics and numerical modeling methods.

framework as shown in Fig. 2 is proposed to simulate the gas atomization process in this paper. The modeling procedure consists of two steps: (1) modeling the primary breakup of melt stream using the VOF method in OpenFOAM; (2) modeling the secondary breakup of primary droplets using the DPM method in Ansys Fluent. For the primary breakup regime, it is important to track the dynamic interaction between the melt stream and the cold gas jet, the formation of liquid ligament, and its breakup into primary droplets. It is found that the VOF method provided by the OpenFOAM InterFoam package is a very robust and flexible package for primary breakup modeling. The droplets tracked by the VOF method in OpenFOAM can be extracted and expressed in the form of discrete points with information on sampling time, position, size, velocity, etc. For the secondary breakup regime, the primary droplets interact further with the high-speed gas flow. Secondary breakup occurs due to the fast-growing liquid-gas interface instability resulting from the competing action of the aerodynamic dragging forces (determined by the relative speed between the droplets and the surrounding gas) against the droplet surface tension. Various secondary breakup models in Ansys Fluent are built for different breakup conditions and mechanisms. After the secondary breakup, the droplet size becomes smaller and smaller. It also becomes more costly and difficult to resolve the shape of every individual droplet. Assuming the droplet is spherical, the Lagrangian method (Fluent DPM model) is adopted to track the droplet size, position, velocity, temperature, and so on. The solidification of droplets can also be considered by accounting for the variation of material properties (density, viscosity, surface tension, specific heat, and heat of fusion) with droplet temperature. In a practical situation of the gas atomization process, there is no cutting boundary between the primary and the secondary regimes. In most cases, there is a transition regime for them. From the modeling point of view, these two methods should be coupled with each other to integrate fully the flow physics of two atomization regimes. Specifically, the information of the droplets tracked using the VOF method for the primary breakup modeling should be extracted and passed to the Lagrangian model for the secondary breakup modeling.

2.2. *Numerical modeling of primary breakup*

The primary breakup occurs inside the atomization chamber near the tip of the close-coupled gas atomization type nozzle, where the molten alloy stream from the melt orifice is disintegrated by the high-speed cold

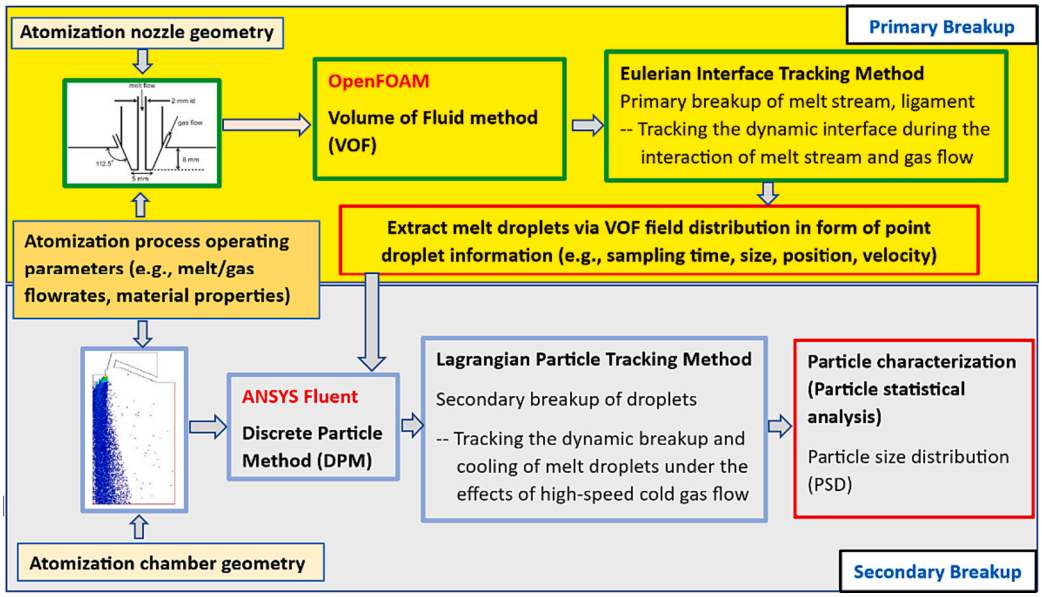

Fig. 2. Numerical modeling framework for the gas atomization process.

gas flow from the exit slit of the gas die nozzle. A CFD-based multiphase flow model for simulating the primary breakup process of the melt stream into primary droplets is constructed to capture the dynamic disintegration of the gas-liquid interface. The computational domain as shown in Fig. 3(a) consists of a 10-degree cylindrical sector of the atomization chamber including both the supply tube for the molten alloy stream and the exit slit of the atomization gas flow. To capture the liquid/gas interface dynamic of the primary droplets produced, the mesh size for the computational domain should be fine enough and at a similar length scale as the droplet diameter. To simplify the CFD model with a focus on modeling the primary breakup process, the atomization gas expansion through the flow channel from the high-pressure gas chamber to the atomization chamber is ignored. Instead, a compressible gas flow model as shown in Fig. 3(b) is applied to estimate the atomization gas flow condition at the exit slit of the gas die nozzle, which is used as the input boundary for the CFD model for simulating the primary breakup process. Therefore, the gas flow within the computational domain of the CFD model for primary breakup modeling can be assumed to have a constant density, i.e., incompressible. Here, a VOF multiphase flow model implemented in the OpenFOAM framework, InterFoam, is adopted to simulate the gas-liquid interface dynamics and the primary breakup in the gas atomization process.

With the assumption of incompressible flow inside the computational domain, the conservation equations of mass and momentum, and the advection of the volume fraction for the two-phase flow of the molten alloy and the atomization gas are as follows,

$$\frac{\partial u_i^m}{\partial x_i} = 0 \tag{1}$$

$$\frac{\partial(\rho^m u_i^m)}{\partial t} + \frac{\partial\left(\rho^m u_j^m u_i^m\right)}{\partial x_j} = -\frac{\partial p}{\partial x_i} + \frac{\partial}{\partial x_j}\left(\tau_{ij}^m - \tau_{ij}^{sg}\right) + F_i^S + \rho G_i \tag{2}$$

$$\frac{\partial \alpha}{\partial t} + \frac{\partial\left(u_j^m \alpha\right)}{\partial x_j} = 0 \tag{3}$$

where u^m, ρ^m is the velocity and density of multiphase flow fields, respectively. p is the pressure field. α is the phase volume fraction with $\alpha = 0$ for gas (g) and $\alpha = 1$ for liquid (l). τ_{ij}^m is the resolved viscous stress tensor and τ_{ij}^{sg} sub-grid-scale stress tensor. Large Eddy Simulation (LES) is used to solve large-scale eddies while modeling small-scale eddies. G is the gravitational acceleration rate, and F^s is surface tension force on the liquid-gas interface.

The viscos stress tensor τ_{ij}^m is defined as

$$\tau_{ij}^m = \mu^m\left(\frac{\partial u_i^m}{\partial x_j} + \frac{\partial u_j^m}{\partial x_i}\right) \tag{4}$$

where μ^m is the mixture viscosity and defined by the volume fraction average of two phases as

$$\mu^m = \alpha^l \mu^l - \left(1 - \alpha^l\right)\mu^g \tag{5}$$

where superscript l stands for the liquid phase of melt and μ the material property viscosity. Similarly, the mixture density can be estimated as

$$\rho^m = \alpha^l \rho^l - \left(1 - \alpha^l\right)\rho^g \tag{6}$$

The interfacial tension force among the phases is evaluated by the Continuum Surface Force (CSF) method by Brackbill et al. [31],

$$\boldsymbol{F}^s = \sigma\kappa\frac{\nabla\alpha}{|\nabla\alpha|}, \tag{7}$$

where σ is the surface tension coefficient, κ is the local interface curvature, and is estimated as,

$$\kappa = \nabla \bullet \left(\frac{\nabla\alpha}{|\nabla\alpha|}\right). \tag{8}$$

Based on solving the above set of two-phase flow governing Eqs. (1–3), the dynamic distribution of phase volume fraction while the primary breakup of the melt stream is calculated, and the dynamic behavior of the melt-gas interface is predicted. Based on the distribution of melt phase volume fraction, an OpenFOAM post-processing package named "extractEulerianParticles" is used to extract the dynamic droplet properties, such as the sampling time, position, velocity, and size, at the outlet boundary of the computational domain, which is used as the input of initial droplets for the primary breakup modeling.

2.3. Numerical modeling of secondary breakup of droplets and particles

After the primary breakup of the melt stream, the droplets will be driven further by the cold high-speed atomizing gas flow leading to secondary breakup, cooling, and solidifying. Solidified particles will be collected at the bottom outlet of the atomization chamber. To simulate

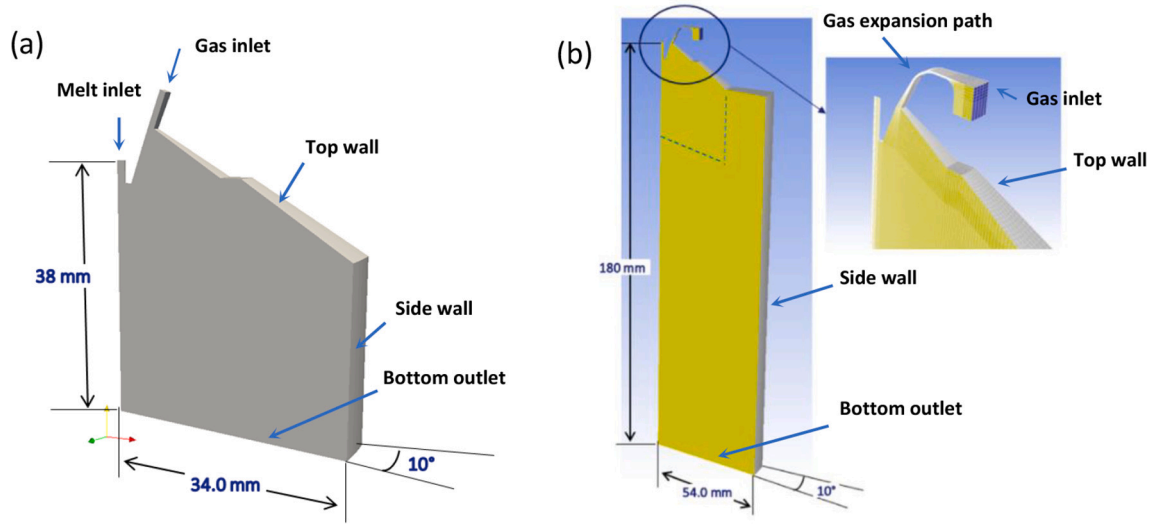

Fig. 3. (a) A CFD model for simulating the primary breakup of the melt stream into droplets using OpenFOAM, and (b) a CFD model for simulating the secondary breakup of the droplets using Ansys Fluent. The model for the primary breakup modeling shown in (a) geometrically overlaps with the model for the secondary breakup modeling at the region near the gas atomization nozzle as indicated by the dashed lines shown in (b).

the secondary breakup process, the Discrete Phase Model (DPM) based on the Lagrangian-Eulerian two-phase flow method in Ansys Fluent is adopted.

2.3.1. Eulerian formulation for gas flow

The atomization gas (Argon), flowing from the high-pressured gas die nozzle to the low-pressured atomization chamber, is considered compressible. The gas flow is governed by the following conservation equations for mass, momentum, and energy,

$$\frac{\partial \rho^g}{\partial t}+\frac{\partial \rho^g\, u_j^g}{\partial x_j}=0 \tag{9}$$

$$\frac{\partial \rho^g u_i^g}{\partial t}+\frac{\partial\left(\rho^g u_j^g u_i^g\right)}{\partial x_j}=-\frac{\partial p}{\partial x_i}+\frac{\partial}{\partial x_j}\left(\tau_{ij}-\tau_{ij}^{sg}\right)+\rho^g G_i+S_{d,i} \tag{10}$$

$$\frac{\partial \rho^g h^g}{\partial t}+\frac{\partial\left(u_j^g h^g\right)}{\partial x_j}=\frac{\partial}{\partial x_j}\left(\frac{k_t}{C_p^g}\frac{\partial T^g}{\partial x_j}\right)+S_h \tag{11}$$

where superscript g stands for the continuous gas phase flow, which is described using the Eulerian formulation method. u,p, h, T are the fields of velocity, pressure, enthalpy, and temperature respectively. ρ, k_t, $C_p$are the material properties of density, thermal conductivity, and specific heat, respectively. G represents the gravitation acceleration rate. S_d and S_h are the momentum and energy source terms due to drag and heat exchange between the dispersed phase (droplets/particles) and continuous carrier gas phase. τ_{ij} is the resolved viscous stress tensor and τ_{ij}^{sg} denotes the sub-grid scale eddy viscosity modeled through large eddy simulation. The definitions of viscosity stress tensor τ_{ij} and enthalpy is given as

$$\tau_{ij}=\mu^g\left(\frac{\partial u_i^g}{\partial x_j}+\frac{\partial u_j^g}{\partial x_i}-\frac{2}{3}\delta_{ij}\frac{\partial u_k^g}{\partial x_k}\right) \tag{12}$$

$$h^g=C_p^g T^g \tag{13}$$

where μ^g is the molecular viscosity of the gas phase.

2.3.2. Lagrangian formulation for droplets/particle

The dispersion of droplets/particles, driven by the high-speed gas flow, is modeled using a Lagrangian framework of the Discrete Phase Model (DPM) in Ansys Fluent. Since the number of droplets produced by the gas atomization process can be massively large, tracking every single droplet is not computationally feasible. The efficient way is to present the discrete droplets by a set of parcels, each one of them represents a group of identical droplets. Lagrangian tracking is performed for parcels instead of individual droplets.

The movement of droplet/particle is tracked in a Lagrangian manner by the following Eqs. [32],

$$d\boldsymbol{x}^d=\boldsymbol{u}^d\,dt \tag{14}$$

$$\frac{d}{dt}\left(\boldsymbol{u}^d\right)=F_D\left(\boldsymbol{u}^g-\boldsymbol{u}^d\right)+\frac{\rho^d-\rho^g}{\rho^d}\boldsymbol{G} \tag{15}$$

where $\boldsymbol{x}^d$ and $\boldsymbol{u}^d$ are the droplet position and velocity, respectively. $\boldsymbol{u}^g$ is the estimated gas velocity at the droplet location. ρ^d and ρ^g are the density of the droplet and gas phase, respectively. $\boldsymbol{G}$ is the gravitational acceleration. The term $F_D\left(\boldsymbol{u}^g-\boldsymbol{u}^d\right)$ is the drag force per unit particle mass from the continuous gas phase and F_D is estimated as

$$F_D=\frac{3\mu^g}{4\rho^d D_d^2}\,C_D\,Re \tag{16}$$

where D_d is the effective diameter of droplets, Re is the Reynold number defined as $Re=\frac{\rho^g D_d\left|\boldsymbol{u}^g-\boldsymbol{u}^d\right|}{\mu^g}$. Assuming droplets are spherical, the drag coefficient C_D can be estimated as

$$\boldsymbol{C}_D=\begin{cases}\frac{24}{Re}\left(1+0.15\,Re^{2/3}\right) & Re<1000\\ 0.424 & Re\geq 1000\end{cases}. \tag{17}$$

Droplet/particle temperature (T_d) is governed by the energy conservation equation,

$$\rho^d\,V_d\,C_p^d\frac{d}{dt}\left(T^d\right)=A_d\,h\left(T^g-T^d\right)+\rho^d\,V_d\,L\frac{d}{dt}\left(f_s^d\right)+A_d\,\varepsilon\sigma\left(\left(T^w\right)^4-\left(T^d\right)^4\right) \tag{18}$$

where T^d, T^g and T^w are the temperatures of droplet/particle, gas flow, and atomization chamber wall, respectively. V_d and A_d are the droplet volume and surface area, respectively. h is the convective heat transfer coefficient between gas and particles, L is the latent heat of solidification, f_s is the solid fraction of droplet/particle, ε is the particle emissivity, σ is the Stefan-Boltzmann constant.

The convective heat transfer coefficient h is calculated by the widely used correlation of Neoli and Gu [21],

$$h=\frac{k_g}{d_p}\left(2+0.6\,Re^{1/2}\,Pr^{1/3}\right) \tag{19}$$

where k_g is the thermal conductivity. Pr is the Prandtl number and defined as $Pr=\frac{C_p^g\mu_g}{k_g}$.

The momentum source terms (S_d) in Eq. (10) and the energy source term (S_h) in Eq. (11) are obtained by summing the drag force and the heat exchange between the dispersed phase and the continuous phase over all droplets,

$$\boldsymbol{S_d}=-\sum\nolimits_d \rho^d F_D\left(\boldsymbol{u}^g-\boldsymbol{u}^d\right) \tag{20}$$

$$S_h=-\sum\nolimits_d\left(A_d\,h\left(T^g-T^d\right)+\rho^d\,V_d\,L\frac{d}{dt}\left(f_s^d\right)\right). \tag{21}$$

In the secondary breakup region of the gas atomization process for powder production, metal droplets go through undercooling, recalescence, peritectic, and segregated solidification before fully solidified [21]. The dynamic changes of droplet/particle temperature are tracked using Eq. (18). The changes in material properties, e.g. density, viscosity, surface tension, specific heat, and solid fraction with temperature can be estimated using the software package Thermo-Calc.

Based on the simulation results, the particles' physical properties such as size, position, velocity, and temperature can be obtained. The particle information at the outlet of the gas atomization chamber is sampled, and then the particle size distribution can be obtained through statistical analysis.

2.4. Secondary breakup model

Five secondary breakup models are developed in Ansys Fluent to simulate the further breakup of droplets in the high-speed gas flow. They are the TAB model, the Wave model, the KHRT model, the Schmehl Breakup model, and the Stochastic Secondary Droplet (SSD) model. The TAB model is based on Taylor's analogy [33] between an oscillating and distorting droplet and a spring-mass system. It is recommended for low-Weber-number injections and is well-suitable for low-speed spray into a stand atmosphere. The Wave model by Reitz [34] considers the breakup of droplets to be induced by the relative velocity between the gas and liquid phases. It assumes that the time of breakup and the resulting droplet size are related to the fastest-growing Kelvin-Helmholtz (KH) instability [35]. The wavelength of the growth rate of the KH instability of the injection jet is used to predict the details of the newly formed droplet. The KHRT model [36] combines the effects of kelvin-Helmholtz waves driven by the aerodynamic forces and the Rayleigh-Taylor instabilities [37] due to the acceleration of shed drops ejected into the gas

flows. Both mechanisms are applied to track the wave growth on the surface of the droplet, and breakup occurs due to the fastest-growing instability based on local conditions. The Schmehl breakup model [38] describes three secondary breakup mechanisms: bag, multimode, and shear for the droplets of a liquid spray. The SSD model [39] treats breakup at high Weber numbers as a discrete random event resulting in a distribution of diameter scales over a range. In the case of gas atomization, both KH and RT instabilities are involved. Therefore, the KHRT model is considered the most suitable model for the simulation of the further breakup of the droplets produced in the primary breakup.

The KH model is based on linear stability analysis of a liquid jet. The eventual breakup and generation of new droplets is due to the fastest-growing mode of the surface waves. The wavelength (λ_{KH}) of the fastest-growing mode and its growing rate (Ω_{KH}) [34,36] was found to be

$$\lambda_{KH} = 9.02\,\frac{\left(1+0.45\,Oh^{0.5}\right)\left(1+0.4\,Ta^{0.7}\right)}{\left(1+0.87\,We_g{}^{1.67}\right)}\,R_d \tag{22}$$

$$\Omega_{KH} = \frac{\left(0.34+0.38\,We_g{}^{1.5}\right)}{(1+Oh)\left(1+1.4\,Ta^{0.6}\right)}\,\sqrt{\frac{\sigma}{\rho^l\,R_d{}^3}}, \tag{23}$$

where R_d is the radius of the primary droplet. Oh is the Ohnesorge number $Oh = We_l{}^{0.5}/Re_l$. Ta is the Taylor number $Ta = Oh\,We_g{}^{0.5}$. Furthermore, $We_l = \rho^l U^2 R_d/\sigma$ and $We_g = \rho^g U^2 R_d/\sigma$ are the liquid and gas Weber numbers, respectively. $Re_l = U\,R_d/\nu_l$ is the Reynolds number. U is the relative velocity between the droplet and the gas phase $U = \left|\boldsymbol{u}^g - \boldsymbol{u}^d\right|$.

The drop lifetime in the presence of growing KH instabilities is defined as $\tau_{KH} = \frac{3.726\,C_{t,KH}\,R_d}{\Omega_{KH}\lambda_{KH}}$, where $C_{t,KH}$ is the KH breakup time constant with a value in a range from 10 to 60. The radius of child droplets produced by KH-breakup is determined by the wavelength of the fastest-growing wave as $R_{c,KH} = C_{KH}\,\lambda_{KH}$, where C_{KH} is the size constant of KH breakup and set to be 0.61.

Similarly, the RT model is based on the wave instability on the droplet surface. The wave frequency of the fastest-growing wave is

$$\Omega_{RT} = \sqrt{\frac{2}{3\sqrt{3\sigma}}\,\frac{\left(-G_t(\rho^l-\rho^g)\right)^{3/2}}{(\rho^l+\rho^g)}} \tag{24}$$

where G_t is the droplet acceleration in the direction of motion. The corresponding wave number is given as

$$K_{RT} = \sqrt{\frac{-G_t(\rho^l-\rho^g)}{3\sigma}}. \tag{25}$$

Breakup occurs when the RT waves have been growing for a time larger than the breakup time $\tau_{RT} = C_{t,RT}/\Omega_{RT}$, where $C_{t,RT}$ is the time constant of RT breakup with a default value of 0.5, and when the wavelength $\lambda_{RT} = 2\pi\,C_{RT}/K_{RT}$ with the fastest growth rate is smaller than the local droplet diameter. The radius of smaller child droplets can be calculated with $R_{c,RT} = \pi\,C_{RT}/K_{RT}$, where $C_{RT}$is the RT breakup radius constant with a default value of 0.1.

2.5. Turbulence model—Large Eddy Simulation for high-speed gas flow

Since high-speed gas flow is applied in the gas-atomization process, a turbulence model is required to model the high-speed gas flow in both stages of primary and secondary breakup. The most common simulation framework within the community is the Reynolds Averaged Navier Stokes (RANS) approach for turbulent gas flow [6,14,19]. In the framework of modeling atomization of liquid spray [32,40,41], Large Eddy Simulation (LES) is applied to simulate the interaction between the turbulent gas flow and liquid droplets. Turbulent flows are characterized by eddies with a wide range of length and time scales. The largest eddies are typically comparable to the characteristic length of mean flow (e.g. shear layer thickness). The smallest eddies are responsible for the dissipation of turbulence kinetic energy. The turbulent flow energy cascades from large to small scales through the interaction of eddies. The large eddies may interact with droplets posing strong effects on the breakup and size distribution. In LES, large eddies are resolved directly, while small eddies are modeled. Hence, the basic governing equations for gas flows are spatially filtered [42]. The filtering of the linear terms leads to the same terms for the filtered variables. In contrast, the filtering of the non-linear terms leads to similar terms with the filtered variables with additional sub-grid scale (SGS) terms which cannot be expressed in terms of the filtered variables due to the nonlinearity of the governing Eqs. [43]. The sub-grid scale stress resulting from the filtering operation is unknown and requires modeling. It can be computed through the Boussinesq hypothesis [42] as,

$$\tau_{ij}^{sg} - \frac{1}{3}\tau_{kk}\delta_{ij} = -2\,\mu_t\,S_{ij} \tag{26}$$

where μ_t is the sub-grid scale turbulent viscosity. The isotropic part of the sub-grid scale stresses $\tau_{kk}$is not modeled but added to the filtered static pressure term. S_{ij} is the rate-of-strain tensor for the resolved scale defined as,

$$S_{ij} = \frac{1}{2}\left(\frac{\partial u_i}{\partial x_j} + \frac{\partial u_j}{\partial x_i}\right) \tag{27}$$

Both Ansys Fluent and OpenFOAM offer different models for the sub-grid scale turbulent viscosity μ_t. In this study, the Wall-Adapting Local Eddy-Viscosity (WALE) model is selected for the eddy viscosity,

$$\mu_t = \rho\,L_s{}^2\,\frac{\left(S_{ij}^d S_{ij}^d\right)^{3/2}}{\left(S_{ij}\,S_{ij}\right)^{5/2} + \left(S_{ij}^d S_{ij}^d\right)^{5/4}} \tag{28}$$

where L_s is the mixing length for sub-grid scales and it is computed using, $L_s = min\left(\kappa\,d, C_w\,V^{1/3}\right)$. Here, κ is the von Karman constant, d is the distance to the closest wall, V is the volume of the computing cell, and C_w is the WALE model constant with a default value of 0.325. The definition of S_{ij}^d in the WALE model in Eq. (28) is given as,

$$S_{ij}^d = \frac{1}{2}\left(g_{ij}^2 + g_{ji}^2\right) - \frac{1}{3}\delta_{ij}g_{kk}^2, \text{ and } g_{ij} = \frac{\partial u_i}{\partial x_j} \tag{29}$$

2.6. Numerical implementation

Following the modeling strategy shown in Fig. 2, two simplified CFD models based on the geometry of the gas atomization nozzle and the atomization chamber are built to simulate the gas atomization process. Fig. 3(a) shows the CFD model for simulating the primary breakup of the melt stream using OpenFOAM. The model consists of a 10-degree cylindrical sector with a radius of 34.0 mm and an axial length of 38.0 mm under the gas atomization nozzle. The relatively small 3D computational domain makes it possible to capture the basic 3D dynamic features in melt stream disintegration and droplet formation with relatively fine mesh grids. The simulation domain is meshed with 386,309 hexahedra elements, and the smallest grid size is about 0.05 mm. The melt inlet is set as a velocity inlet boundary. The gas inlet is set as a volume flow rate inlet boundary. The top wall is set as a nonslip wall boundary. Both the side wall and the bottom outlet are set as pressure outlet boundaries. The solver "InterFoam" in OpenFoam v2212 is applied to solve the governing equations. The time step size is adapted dynamically in the simulation so that the max Corant number is set to 0.6 for fluid flow and 0.3 for VOF field convection, and hence it varies in the range from 1×10^{-9} s to 1×10^{-7} s. The total simulation time is set to 40 ms.

Fig. 3(b) shows the CFD model for simulating the secondary breakup of the melt droplets produced in the primary breakup using Ansys Fluent 19.2. The model consists of a 10-degree cylindrical sector with a radius

of 54.0 mm and an axial length of 180.0 mm of the atomization chamber. The model also includes the high-gas plenum and gas expansion flow path (De-Laval nozzle) with a small throat of 0.05 mm. The simulation domain is meshed with 403,369 hexahedra elements. The gas inlet is set as a pressure inlet boundary. Both the top wall and side wall are set as nonslip wall boundaries. The bottom outlet is set as a pressure outlet boundary. With such settings of the computational domain, a compressible gas model is applied to predict the gas flow from the high-pressure gas plenum to the atomization chamber. It should be highlighted that the model for the primary breakup modeling (as shown in Fig. 3(a)) geometrically overlaps with the model for the secondary breakup modeling at the region near the gas atomization nozzle as indicated by the dashed lines shown in Fig. 3(b). In this case, the droplets produced in the primary breakup modeling can be input into the secondary breakup modeling, which is based on the transient simulations using the Ansys Fluent DPM model. The time step size is set to 5×10^{-6} s the continuous flow phase and 1×10^{-6}s for the discrete particle phase. The total simulation time is set to 40 ms as well. In addition, when the CFD model shown in Fig. 3(b) is set without droplet injections, it can be used to predict the gas flow field under the specified gas atomization pressure

3. Experimental method

3.1. Gas atomization equipment

The gas atomization facility utilized in this study features a VIGA (Vacuum Induction Inert Gas Atomization) atomizer. In this system, the raw materials are loaded into a 1.5-l crucible and melted within a vacuum induction melting (VIM) furnace. Subsequently, they are atomized using an inert gas, accelerated through a De-Laval nozzle, in a close–coupled configuration to the molten metal delivery nozzle, as illustrated schematically in Fig. 1. The maximum temperature within the VIM furnace can be heated to 1700 °C, which is constrained by the use of alumina-based ceramics for both the crucible and the melt delivery tube. Throughout the entire process, it is possible to adjust the atmosphere pressure in both the melting chamber and the atomization tower independently. The vacuum level within both chambers can reach up to 6×10^{-3} mbar. An over-pressure of up to 1.35 bar can be applied exclusively within the melting chamber to favor molten metal flow through the delivery tube and adjust its flow. Before and during the whole atomization process, a dedicated heating unit is used to heat the melt delivery tube to prevent the solidification of molten metal either within the tube or at the exit of the metal delivery nozzle. This apparatus is particularly critical due to the small diameter of the molten metal delivery nozzle, which can be set between 1.5 and 2.5 mm, depending on the chosen processing parameters. The melt temperature control differs between the melting and atomization phases. During melting, temperature is regulated using a thermocouple positioned at the base of the crucible. Conversely, during atomization, temperature is monitored with an optical pyrometer measuring the temperature of the uppermost surface of the molten bath. Following the atomization process, the powders are gathered in two distinct hoppers. The primary hopper contains approximately 90–95% of the powders, while the finer fraction of atomized powders is collected in the secondary hopper after being physically separated from the exhaust gas by a cyclone.

3.2. Experimental procedure and material property

Melt temperature, atomization pressure, and the overpressure applied to the melt delivery tube are the primary parameters to control when gas atomizing a molten metal bath. Melt temperature predominantly affects the viscosity of the molten alloy, facilitating its flow through the melt delivery tube. It should be highlighted that overheating is a critical factor within the atomization process, as it reduces surface tension and promotes secondary breakup mechanisms during atomization [14]. As a general guideline, an overheating of approximately 150 to 200 °C is typically applied to the molten bath when specific data are not available for the alloy to be atomized. However, certain alloys, such as those based on iron, exhibit a lower sensitivity to overheating when considering viscosity reduction as reported in [44]. Due to the lack of experimental data regarding NiSi12% viscosity, a generic 200 °C overheating was employed for the atomization therefore, the molten bath temperature was carefully adjusted to approximately 1350 ± 5 °C. While undergoing atomization, a slight temperature increase, as detected by the pyrometer, was observed, with the highest recorded temperature reaching 1375 °C at the end stage of the atomization process.

Throughout the entire process argon gas served as both the shielding gas in the VIM furnace and the atomization gas in the atomization chamber. While nitrogen is a common choice in industrial practices for atomizing steels and nickel alloys, argon was chosen in this study for its superior inertness. An average atomization pressure of 40 bar was set for the atomization due to previous trials with Nickel alloys. This specific atomization pressure could give a net yield of powder in the 20–63 μm suitable for laser powder bed fusion (L-PBF) between 37 and 42% for stainless steels and Nickel alloys. Low atomization gas pressure can exclude the risk of metal freezing at the melt delivery nozzle and produce coarser powders. When the atomization pressure is increased over 50 bar, finer powders will be produced, and a high risk of instabilities at the nozzle tip could be caused [8].

The flow of molten metal through the melt delivery tube is controlled by the overpressure in the VIM furnace, which is added to the metallostatic pressure acting on the bottom of the crucible. When the flow of atomization gas remains constant, it ensures a consistent gas-to-metal (GMR) ratio. During these tests, the overpressure of 1.25 bar was established just before initiating the atomization process and maintained consistently throughout. As atomization progressed, the metallostatic pressure on the melt delivery tube gradually decreased in concert with the gradual depletion of the crucible contents. These considerations are valid in the absence of a high-speed gas flow from the atomization head located beneath the crucible. However, as indicated in the literature [14], the high velocity of the atomization gas itself creates a suction effect, further altering the flow of molten metal. To account for these factors, the metal flow rate was averaged over the entire atomization process and used as an input for modeling.

3.3. Experimental data analysis method

After unloading the powders from the primary hopper, they underwent mechanical screening to remove any atomization debris, one single sieving pass was enough to remove the large atomization debris. A laboratory test sieve of 200 mm in diameter and 250 μm aperture (60 mesh) compliant with ISO 3310-1 was used (Retsch GmbH, Haan - Germany). Subsequently, they were mixed with powders from the secondary hopper using a tubular mixer to prevent the segregation of the finer particles. The particle size distribution (PSD) of the as-atomized powders was determined using laser diffraction, utilizing a Malvern Mastersizer 3000 equipped with an Aero S dry powder dispersion unit (Malvern Panalytical Ltd., Malvern – UK). A feed rate of 25% and a carrier gas pressure of 2.5 bar of compressed air were selected. To minimize experimental variability, three separate samples were measured three times each. The powder morphology was qualitatively assessed through scanning electron microscopy (SEM) for a sample sieved in the 20–63 μm range suitable for processing by L-PBF. A Zeiss EVO 15 equipped with secondary and backscattered electron probes (Carl Zeiss s.p.a. Milano – Italia) was used.

4. Results and discussion

4.1. Observations of gas atomization tests

Examining the snapshot presented in Fig. 4(a), numerous bright lines emanate from the core of the melt stream. These lines represent the trajectories of relatively large and hot primary droplets. The photograph documents the formation of cold splats, small portions of molten material that do not enter the secondary breakup region. Instead, they are accelerated tangentially to the atomization plume. A detailed examination of the atomization plume at a high frame rate (1200 fps) provides insight into the close interaction between the gas and metal during the disintegration of the molten material.

The frames presented in Fig. 4(b-d) cover an 8-s interval of atomization. While the atomization plume appears stable to the naked eye, the use of high-frame imaging reveals a pulsating behavior [13]. The primary breakup region, where primary ligaments form, is located close to the melt delivery nozzle, within a few millimeters. As a result of this primary breakup, droplets are generated and propelled away from the core region of the melt stream by the high-speed gas flow. The secondary breakup of these primary droplets occurs within 20 to 25 mm from the melt delivery nozzle. Below the melt stream core, a foggy zone with numerous fine droplets/particles is visible, as depicted in Fig. 4(a). These fragmented particles then undergo cooling as they descend along the atomization tower, ultimately collecting in the primary hopper.

Fig. 5 illustrates the morphology of the NiSi12% powders obtained from the gas atomization test. The majority of the particles exhibit an approximately spherical shape, with a small number of satellites indicating optimal conditions for achieving high flowability.

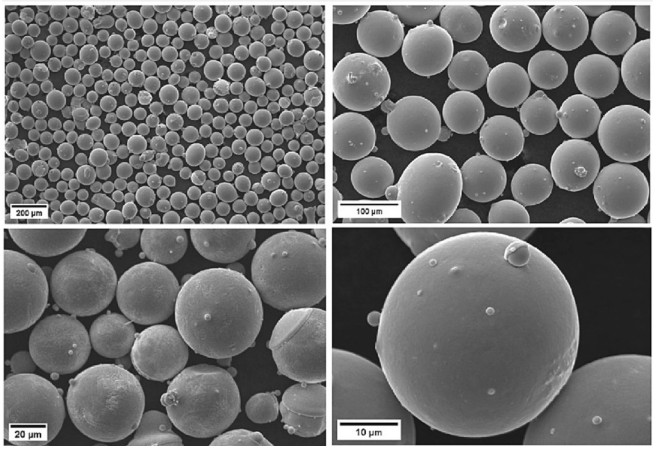

Fig. 5. SEM images of NiSi12% powders produced under the 40 MPa.

A quantitative assessment of powder morphology, conducted using the Malvern Morphologi 4 (Malvern Panalytical Ltd., Malvern – UK), is presented in Fig. 6. Powder circularity best characterizes the sphericity of the powders, while convexity is directly linked to the surface roughness of each analyzed particle and serves as an indicator of the presence of satellites. Both parameters are closely tied to powder size, as

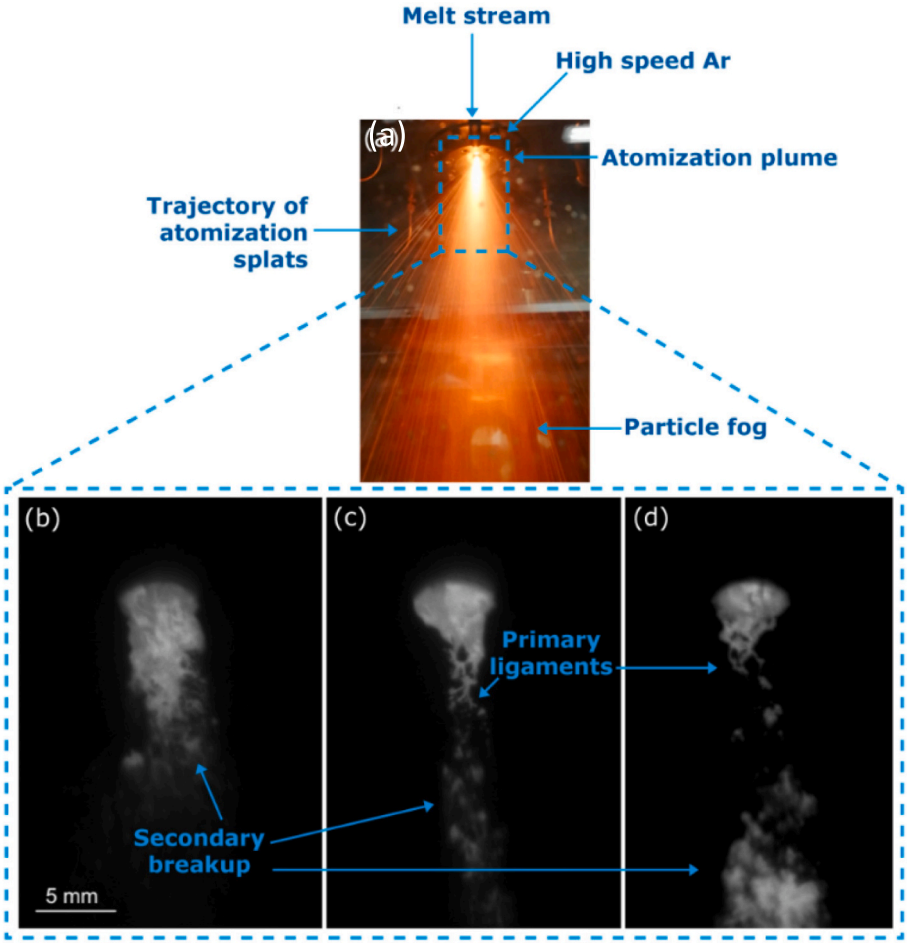

Fig. 4. (a) Overview of the spray pattern formed as the melt stream interacts with the high-speed gas flow in the gas atomization process; (b-d) Snapshots capturing the behavior of the melt-gas interface during the primary breakup of the melt stream and the secondary breakup of droplets using high-speed imaging.

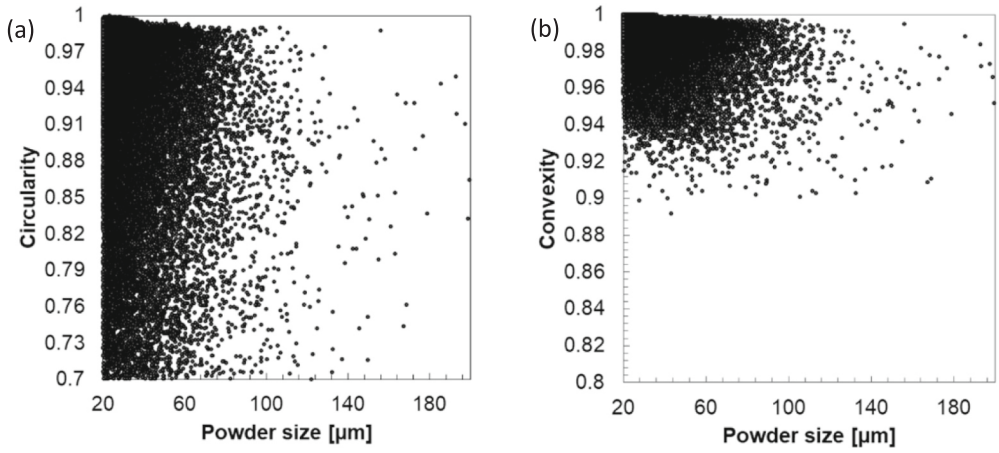

Fig. 6. Quantitative powder morphology; (a) circularity as a function of powder size, (b) convexity as a function of powder size.

observed in Fig. 6. Smaller powders tend to be more spherical with fewer satellites, attributed to the higher surface tension during solidification, which reduces deviations from sphericity.

The metal particle size distribution is analyzed using a laser particle analyzer. The particle size range measured by the laser particle analyzer is (0 μm, 3000 μm), which is much larger than the size range (0 μm, 200 μm) we are interested in this study. Fig. 7(a) shows the particle volume ratio/frequency for different size groups within the particle size range (0 μm, 200 μm) obtained by a laser particle analyzer. The bin size for the particle size analysis increases exponentially which is more suitable for logarithmic scale plots of particle size distribution. Hence, the particle size distribution ($p_s{}^i$) given by the laser particle analyzer depends on the selection of bin size with a size range ($s_1{}^i, s_2{}^i$). To make the particle size distribution independent of bin size and easy to compare with those obtained in simulation, it is better to use normalized differential frequency density instead of volume ratios within selected bins. The differential frequency density ($\rho_s{}^i$) for the particles within the bin b^i with a size range ($s_1{}^i, s_2{}^i$) is calculated from the volume ratio/frequency ($p_s{}^i$) as $\rho_s{}^i = p_s{}^i/(s_2{}^i - s_1{}^i)$. In addition, the particle size distribution within the interested size range (0 μm, 200 μm) is also normalized so that $\int_{0\ \mu m}^{200\ \mu m} \rho_s{}^i d(s^i) = 100$. With such processing, the updated particle size distribution in terms of normalized differential frequency density is shown in Fig. 7(b).

4.2. Simulation results of reference case

To evaluate the effectiveness of the proposed numerical modeling framework for the gas atomization process, numerical modeling is used to predict the droplet formation at the primary breakup stage, the secondary breakup of the primary droplets, and the particle size distribution under the reference test conditions presented in Section 4.1. The gas atomization reference test is designed to produce NiSi12% alloy powders.

4.2.1. Primary breakup of melt stream

For the reference test, the melt stream mass flow rate was calculated by dividing the total weight of alloy loaded in the crucibles over the atomization period. The estimated melt flow rate was 1.26 kg/min. The gas atomization pressure was operated at 40 MPa. The gas flow rate was obtained by measuring the mass consumption rate of atomization gas (argon), and it was about 2.28 kg/min on average. The gas density at the region near the outlet of the gas flow path from the gas plenum was estimated by a CFD modeling of the compressible single gas phase flow. The material properties of NiSi12% melt were estimated using the Thermo-Calc software and listed in Table 1. With the above-mentioned inlet flow rates and material properties of both melt and gas phases, the primary breakup model described in Sections 2.2 and 2.6 and implemented in OpenFOAM can be configured to run the simulation.

Table 1
Material properties for the primary breakup modeling.

Material	Density (kg/m^3)	Kinematic viscosity (m^2/s)	Surface tension (N/m)
NiSi12% melt	7441.56	1.20E-6	1.26
Argon gas	Ideal gas law	2.74E-5	

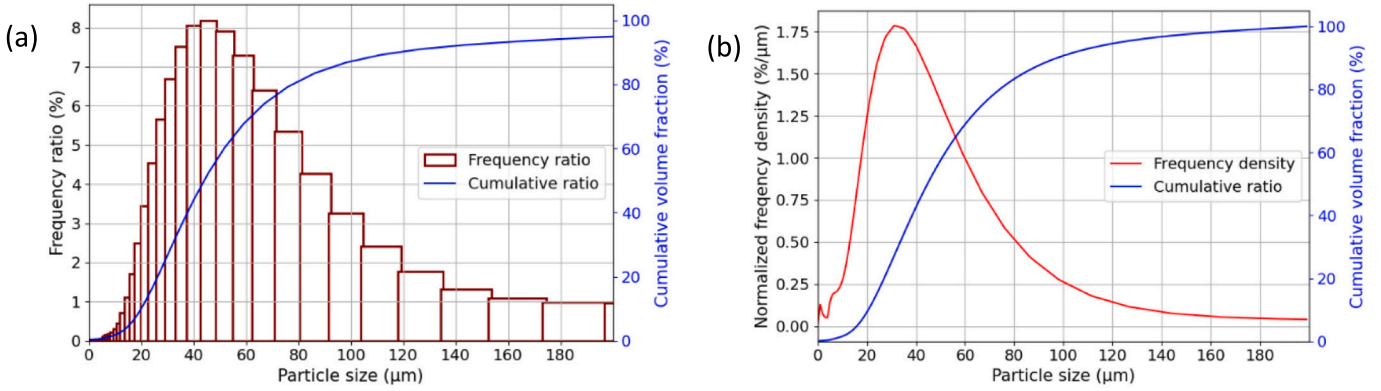

Fig. 7. Particle size distribution within the size range (0 μm, 200 μm) in the form of (a) volume ratio/frequency and (b) the normalized differential frequency density. The cumulative particle size distribution is also displayed.

A series of predicted snapshots of the disintegration of the melt stream by the high-speed gas flow at a time interval of 0.2 ms are shown in Fig. 8. Fig. 8(a-c) shows the growth of a ligament under the melt nozzle tip. The melt ligament becomes longer and longer while the length of the melt stream core becomes shorter due to the local circulating gas eddy under the melt nozzle tip. Fig. 8(d-f) shows the disintegration of the ligament into droplets. Fig. 9 shows the detailed interaction process between the ligament and the high-speed gas flow. Fig. 9(a) shows that the high-speed gas impinges on the ligament from the upstream side, and there are several local circulating eddies on the downstream side. Then, the ligament breaks into several sections as shown in Fig. 9(b). The high-speed gas breaks these ligament sections further into droplets and drives them downstream as shown in Fig. 9(c). Finally, the ligament is pinched off the melt stream core, which resumes to an inverted cone shape under the nozzle tip as shown in Fig. 9(d). When the dynamic behavior of the melt-gas interface predicted by the numerical simulation shown in Fig. 9 is compared qualitatively with that captured by a high-speed imaging technique shown in Fig. 4(b-d) and the work of [13], they show similar features.

It can be concluded from Fig. 9 that the interaction of gas flow eddies with the melt stream plays a very important role in the primary breakup process. The instability of the melt stream also affects the formation of gas flow eddies. The typical snapshots of the gas-speed distribution under the atomization nozzle are shown in Fig. 10. Since the Large eddy simulation turbulence model is adopted, gas flow eddies and fluctuations are predicted by the model, which posts strong effects on the instability on the surface of the liquid core leading to the primary breakup. It is believed that the Large Eddy Simulation is important in reasonably capturing the detailed flow physics of the primary breakup process [27].

The droplets tracked by the VOF function are sampled at the bottom outlet of the computational domain, converted into point particles, and stored with the information of sampling time, diameter, position, and velocity. A statistical analysis of the sampled droplets gives the size distribution as shown in Fig. 11. The melt stream is well disintegrated into droplets smaller than 300 μm in diameter. The droplets produced in the primary process have the highest frequency density at a size of around 120 μm.

Since the physical boundary for the primary breakup zone in the gas atomization process cannot be clearly defined, the simulation results depend upon the selections of the computational domain and mesh grid size. It is difficult to verify the simulation results with the experimental observations. To follow the basic mass conservation law, the size of the sampled droplets is adjusted so that the melt flow rate of the total droplets is the same as the one applied in the reference test. The sampled droplets are used as one of the key inputs to the modeling of the secondary breakup inside the atomization chamber.

4.2.2. *Secondary breakup of melt droplets*

The secondary breakup model is described in Sections 2.3, 2.4, and 2.6 and implemented in Ansys Fluent. Since a compressible ideal gas model is applied, the atomization gas pressure of 40 MPa is set to the inlet to the gas plenum. The total gas consumption rate predicted by the model agrees well with the measurement in the reference test. The droplets sampled at the primary breakup modeling stage are input into the model for the secondary breakup modeling. The KHRT secondary breakup model implemented in Ansys Fluent is applied to track the breakup of the primary droplets into fine droplets until the droplet surface is stable, which can be estimated by the droplet Weber number. The melt density, viscosity, and surface tension coefficient can vary with the droplet temperature. Hence, the cooling of droplets by the atomization gas flow can have a strong effect on the final particle size distribution. The variations of the melt thermal properties with temperature are estimated using Themo-Calc as shown in Fig. 12.

Fig. 13(a) shows a snapshot of the predicted velocity magnitude distribution of the high-speed gas flow from the gas plenum to the atomization chamber. Since the Large Eddy Simulation turbulence model is applied, the gas flow fluctuations and eddies are predicted inside the atomization chamber. Fig. 13 (b) shows a snapshot of droplet/particle distribution inside the atomization chamber. After the primary droplets

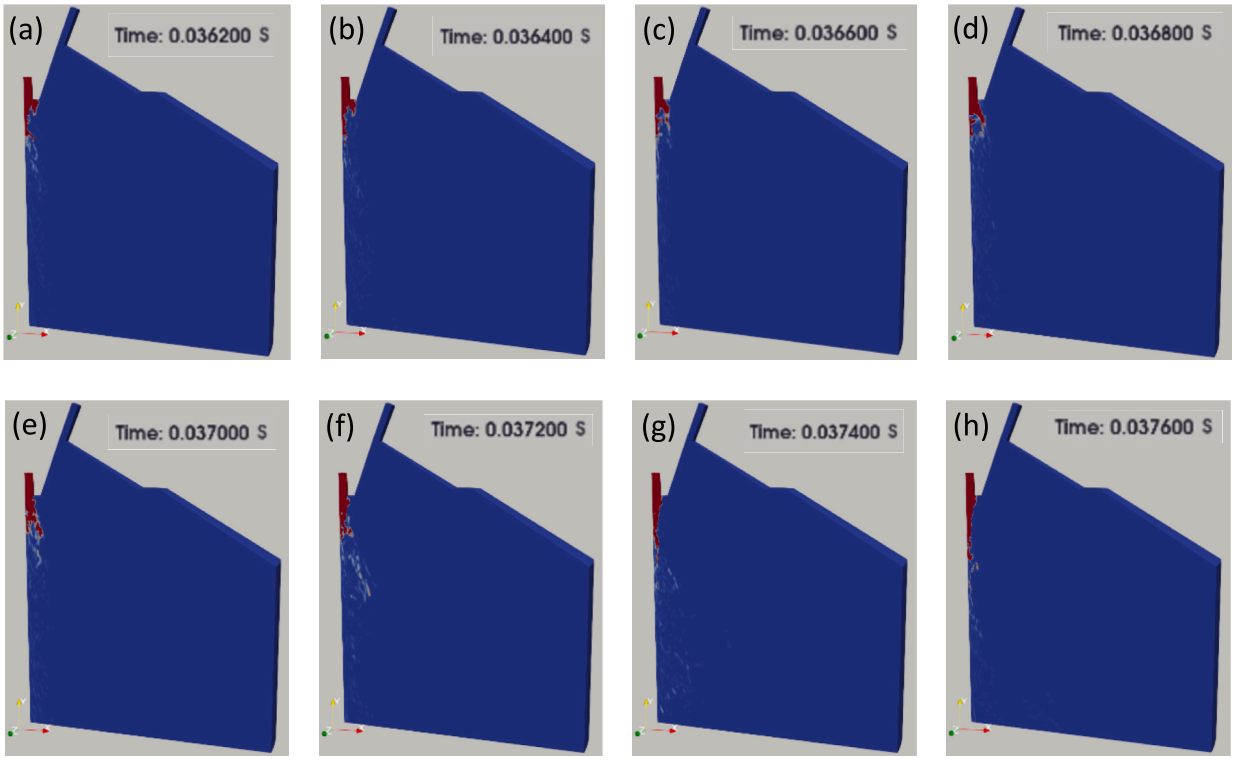

Fig. 8. Model prediction of gas-liquid interface dynamic deformation and droplet formation due to primary breakup.

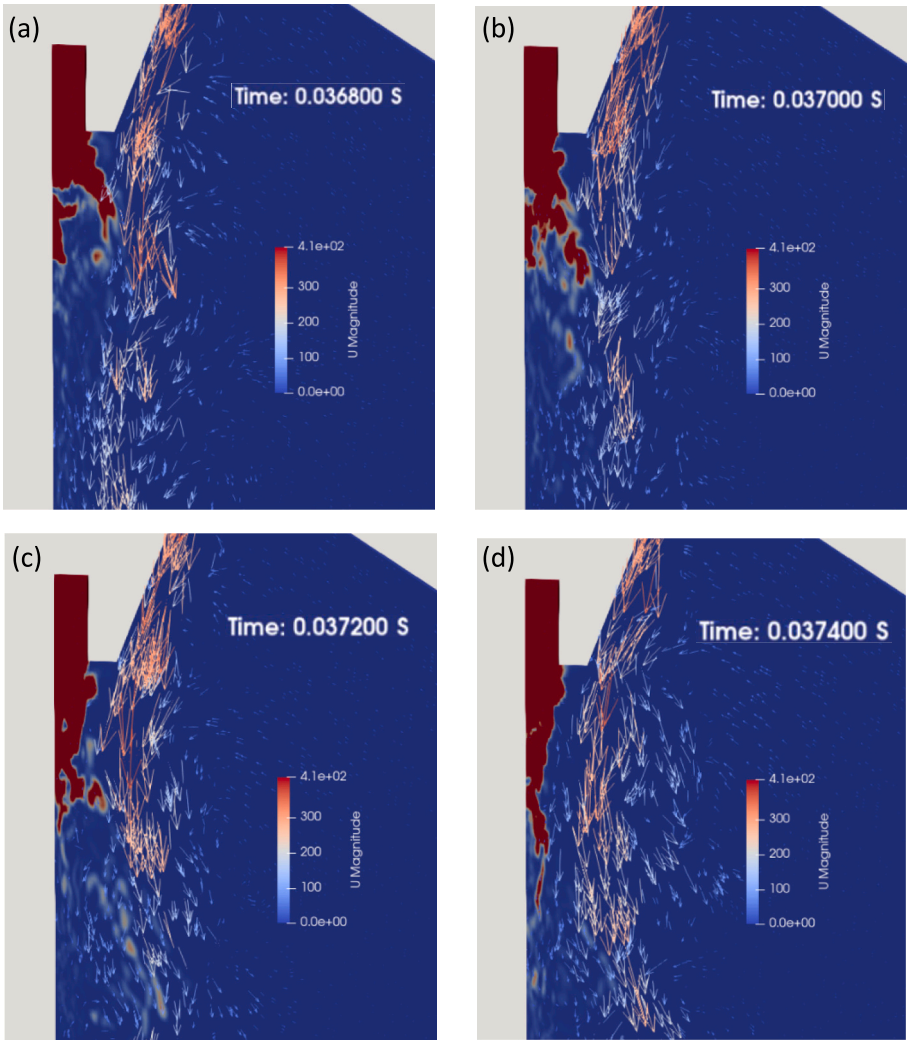

Fig. 9. Model predictions on the detailed interaction process between the melt ligament and high-speed gas flow, and the breakup into droplets.

are input into the model, the high-speed gas creates a strong drag on the droplets leading to further break up into smaller droplets. The particles are transported and cooled by the gas flow to the downstream.

4.2.3. Particle size distribution

Particles are sampled at the outlet boundary of the atomization chamber during the transient simulation of the secondary breakup process. The statistical analysis is performed for the sampled particles to extract the particle size distribution. Fig. 14 shows the comparisons of the final particle size distribution predicted by the numerical model and the measurement for the reference test. They are in good agreement in the size range (0 μm, 200 μm). The model made slightly under-prediction for small particles (< 25 μm) and over-prediction for large particles (> 100 μm).

In addition, two additional gas atomization tests are performed with the operating conditions: (a) gas atomization pressure at 35 MPa, gas flow rate at 2.18 kg/min, and melt flow rate at 1.92 kg/min; (b) gas atomization pressure at 45 MPa, gas flow rate at 2.57 kg/min and melt flow rate at 1.43 kg/min. The particle size distributions of the powders are compared with those predicted by the numerical model as shown in Fig. 15. In general, the particle size with the largest frequency density predicted by the numerical model agrees well with those observed in the experiment.

To quantitatively evaluate the numerical model prediction accuracy of particle size distribution, the following deviation metric methods are applied. Based on the cumulative volume fraction of particle size distribution, the percentile values of D10, D50, and D90 are checked. Based on the normalized frequency density (ρ_s^i), a relative prediction error (E_{rel}) and an absolute prediction error(E_{abs}) are defined as

$$E_{rel} = \frac{\sqrt{\sum_{i=1}^{i=N}\left(\rho_{s,sim}^{i} - \rho_{s,exp}^{i}\right)^2 \Big/ N}}{MAX\left(\rho_{s,exp}^{i}\right)} \tag{30}$$

$$E_{abs} = \frac{1}{100}\int_{i=1}^{i=N}\left|\rho_{s,sim}^{i} - \rho_{s,exp}^{i}\right| d\left(s^{i}\right). \tag{31}$$

The model prediction accuracy of the particle size distribution for the gas atomization tests is summarized in Table 2. From the cumulative volume fraction distributions, it can be concluded that the model makes good predictions of D50 for all three gas atomization tests. For Test case A, the model underestimates the frequency density for small particles (<40 μm) as shown in Fig. 14(a), and the D10 is pretty overestimated. For Test cases B and C, the model overestimates the frequency densities for large particles (> 100 μm) as shown in Figs. 13 and 14(b), and the D90s are quite overstimated. Interpreted from the frequency density distributions, the numerical model makes better predictions for Test cases B and C in terms of the relative error (E_{rel}), while better predictions for Test cases A and B in terms of the absolute error(E_{abs}).

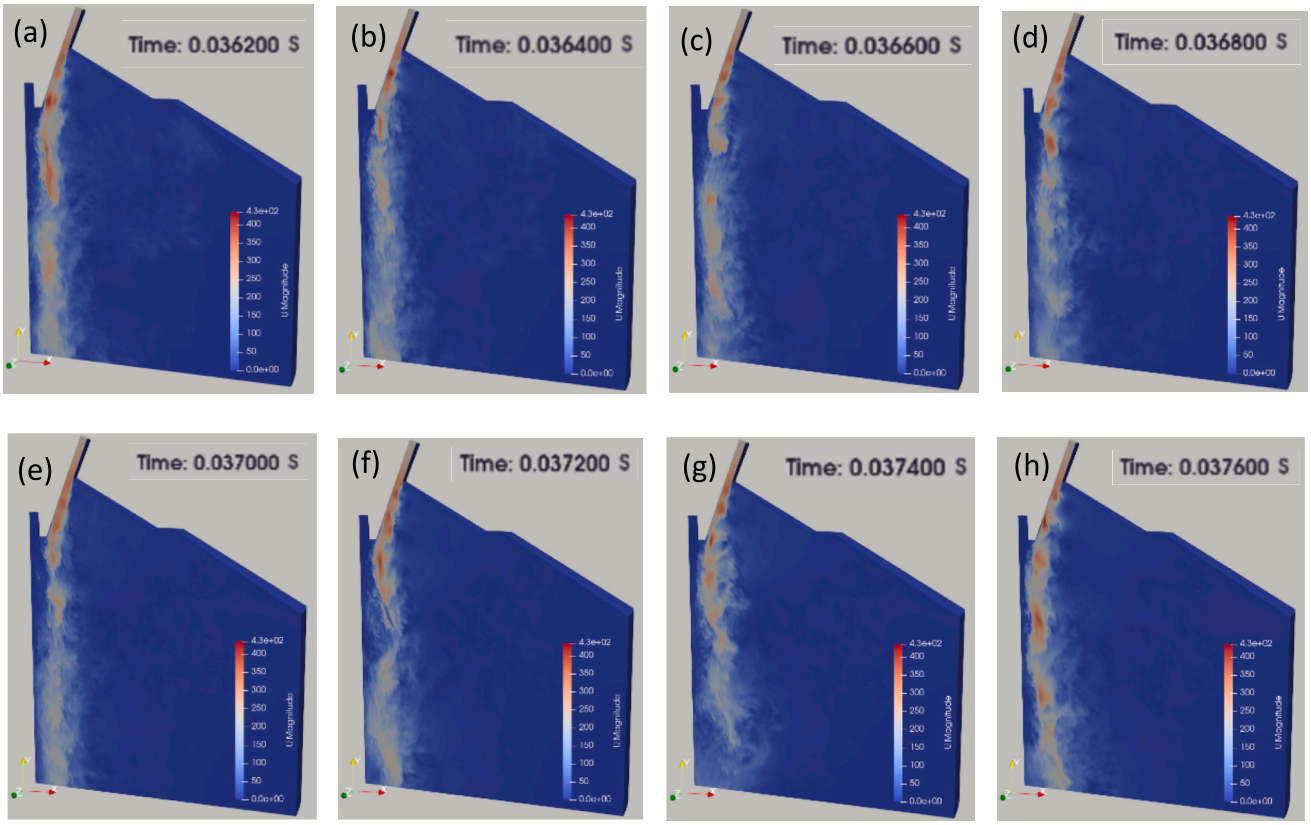

Fig. 10. Model prediction of the temporal distributions of the gas flow magnitude and flow eddies in the primary breakup process.

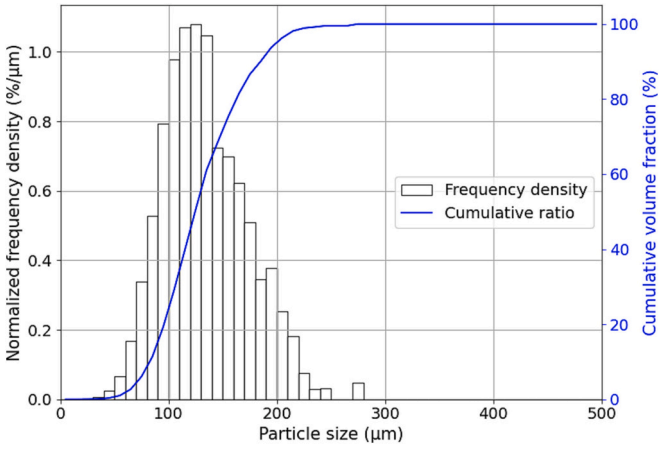

Fig. 11. Predicted droplet size distribution after the primary breakup.

4.3. Model sensitivity study on effects of operational parameters on particle size distribution

4.3.1. Secondary breakup models

Ansys Fluent offers five sub-models for droplet secondary breakup as described in Section 2.4. Each sub-model under certain assumptions includes certain mechanisms for secondary breakup. A sensitivity study of these secondary breakup sub-models was performed to identify which model is more suitable for simulating the droplet breakup in the gas atomization process. Fig. 16 shows the variation of particle distribution predicted by different sub-models for the secondary breakup under the conditions of the reference gas atomization test. The particle size distributions predicted by both the KHRT and the WAVE models are quite similar, which is also close to the one measured in the gas atomization test. Both models underestimate the frequency density for the particles with diameters smaller than 22 μm. The prediction of the Schmehl model shows the smaller-sized particles within the diameter range of 12–24 μm have the highest frequency density. The SSD model overestimates the frequency density of the larger-sized particles compared to the reference test. The TAB model makes a reasonable prediction of the frequency density for particles smaller than 32 μm, over-prediction for particles within the range of 32–56 μm, and under-prediction for particles within the range of 56–140 μm. Referring to the detailed description of the KHRT model in Section 2.4, it is believed the KHRT model is more suitable for simulating the secondary breakup of droplets in the gas atomization process. The KHRT model is therefore applied in other simulations presented in this paper.

4.3.2. Effect of gas atomization pressure

When the operating pressure for the gas inlet plenum is varied at $P_G = 30, 35, 40, and\ 45$ bar in the simulations, the gas flow rates predicted by the compressible single gas phase model are 1.71, 1.98, 2.28, and 2.55 kg/min, respectively. It is confirmed that the model predictions on the gas flow rates agree well with the measurements in the reference gas atomization tests where $P_G = 40$ bar. To study the effect of gas atomization pressure on the particle size distribution, the inlet flow rate of melt is artificially kept constant at 1.26 kg/min in the simulations. Fig. 17 shows the particle size distribution after secondary breakup under different inlet gas operating pressures. As the inlet gas operating pressure increases from 30 bar to 45 bar, the mass flow rate of gas increases as well as the gas flow speed. Due to the higher momentum in the gas flow, the melt stream can be broken into smaller droplets. As the inlet gas operating pressure increases from 40 bar to 45 bar, more small particles are generated, but there is no significant change in particle size with the highest frequency density.

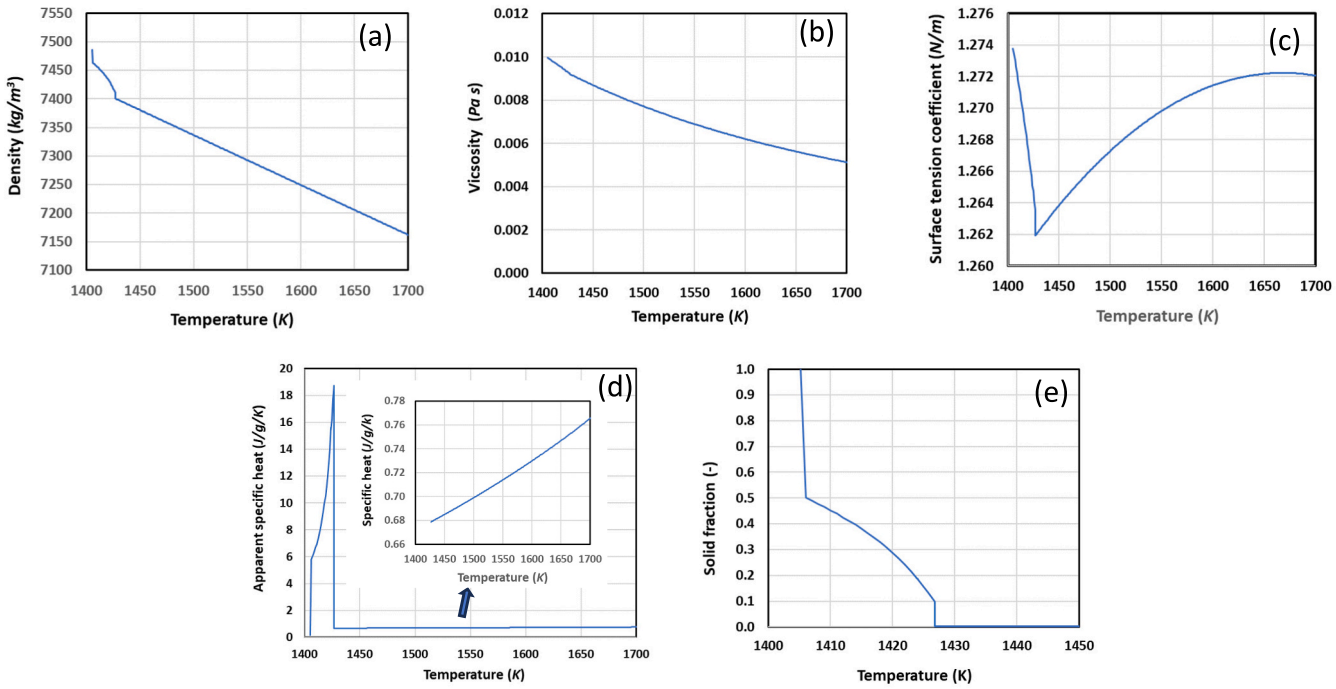

Fig. 12. Variations of the melt (NiSi12%) thermal properties: (a) density; (b) viscosity; (c) surface tension; (d) specific heat; (e) solid fraction with temperature estimated using Thermo-Calc.

4.3.3. *Effect of melt inlet flow rate*

If the gas atomization pressure is fixed at 40 bar, the effect of melt flow rate on particle size distribution in the gas atomization process can be investigated through simulations. Referring to the melt flow rate in the reference gas atomization test: $\dot{m}_{l,ref} = 1.26\,\mathrm{kg}/min$, the melt flow rates can be varied at different ratios: $\dot{m}_l/\dot{m}_{l,ref} = 0.5, 1.0$ and 1.5. The distributions of particle size predicted by the simulations with different melt flow rates are shown in Fig. 18. When the melt flow rate is increased by 50% to the reference test, there is no significant change in the particle size distribution. However, when the melt flow rate is decreased by 50% to the reference test, the particle size increases slightly. Luo et al. [13] experimentally investigated the breakup behavior of the liquid jet in the gas atomization for powder production. Hua et al. [45] numerically studied the microdroplet formation in coflowing immiscible liquids. Different breakup modes for the liquid stream: dripping and jetting, are reported. The dripping mode occurs when the surface tension is strong and intends to attach the droplet to the small liquid delivery tube. It happens when the liquid stream flow rate is low and the dragging force from the external fluid flow is not strong enough. In the contrary situation, the liquid stream breaks up in the jetting mode. Normally, the droplet size produced in the dripping mode is relatively larger than that in the jetting mode. The droplet size variation can be larger in the dripping mode than that in the jetting mode. This helps to explain the simulation results about the effects of melt flow on the particle size distribution.

4.3.4. *Effect of melt viscosity*

The melt viscosity can vary significantly with the changes in droplet temperature while the droplet is cooled and solidified inside the atomization chamber. The variation of melt viscosity also has strong effects on the breakup behavior of the melt stream into droplets. Fig. 19 shows the droplet size distribution after secondary breakup under different melt viscosity ratios. The melt droplet is more difficult to break up with a higher viscosity according to the secondary breakup model described in Section 2.4. Melt with higher viscosity produces larger droplets/particles through gas atomization. With the increased melt viscosity, the particle size with the highest frequency density becomes larger. The frequency density for small particles (< 60 μm) decreases while for large particles (>100 μm) increases. Hence, the powders will have a wider size range.

4.3.5. *Effect of melt surface tension*

The melt surface tension is one of the important forces to retain the droplets from breakup. The melt surface tension can also be temperature-dependent. As the temperature decreases, the surface tension coefficient will decrease before the melt starts to solidify and increase significantly during the solidification process as shown in Fig. 12. Hence, the variation of the melt surface tension coefficient can significantly affect the final particle size distribution in the gas atomization process. Fig. 20 shows the droplet size distribution after secondary breakup under different surface tension ratios. The melt droplet is more difficult to break up with a higher surface tension. Melt with higher surface tension produces larger droplets/particles through gas atomization. The melt with smaller surface tension produces smaller particles with a relatively narrow size distribution.

4.3.6. *Effect of melt superheat temperature*

Since both melt viscosity and surface tension are temperature-dependent, the melt droplet breakup dynamics are affected by the changes in temperature. During the secondary breakup process, the droplet size becomes smaller. The smaller droplets can be cooled more effectively by the high-speed cold gas. Hence, the secondary breakup process of melt droplets can be affected by the cooling and solidification processing significantly. The cooling dynamics of the melt droplets can be considered in the Fluent DPM model for the secondary breakup.

Fig. 21 shows the particle size distribution after the secondary breakup under different melt superheat temperatures of 1600 K, 1500 K, 1450 K, and 1430 K. When the melt superheat temperature is 1600 K, it is about 200 K higher than the liquidus temperature. The secondary breakup of the melt droplet occurs while its temperature is above the liquidus temperature. This means the droplet becomes fully broken up before the solidification process starts. In this case, the mean particle

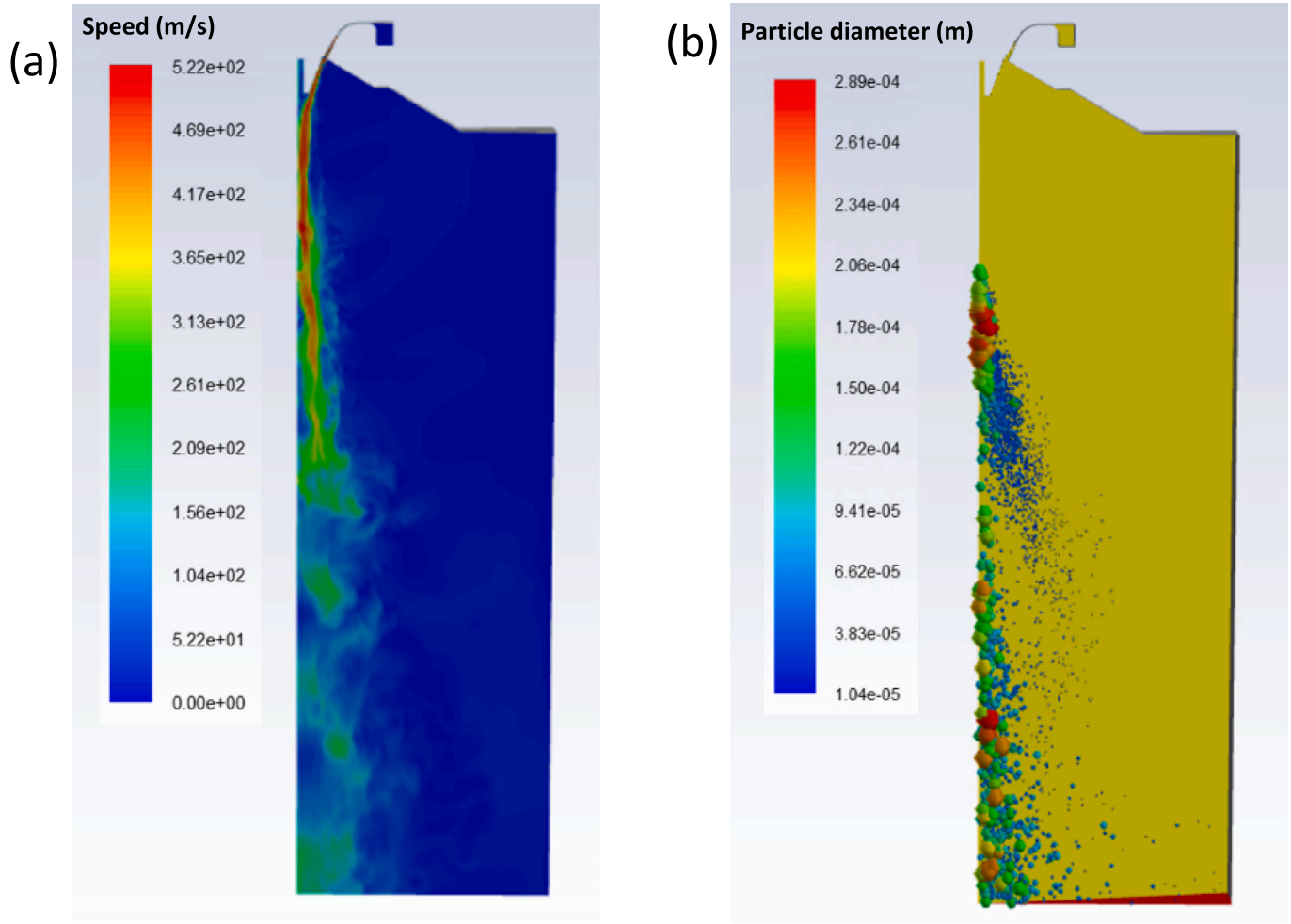

Fig. 13. A snapshot of model prediction of the distributions of (a) the gas flow velocity magnitude and (b) particles (colored by diameter) inside the atomization chamber in the secondary breakup process.

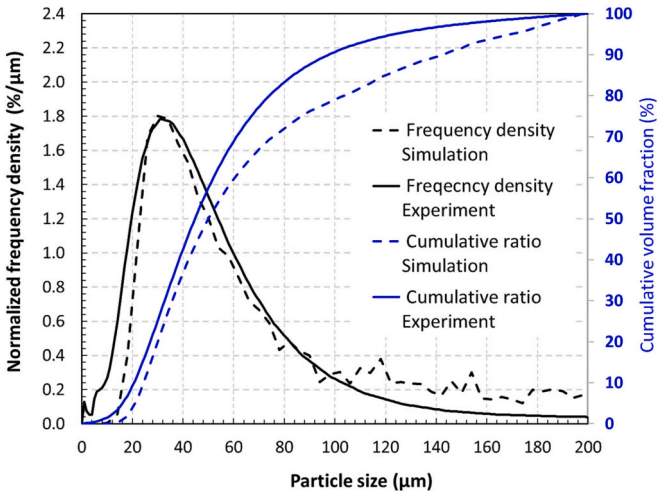

Fig. 14. Comparison of the particle size distributions in the form of normalized frequency density and cumulative volume fraction predicted by the numerical model and those measured in the reference gas atomization test. The gas atomization pressure is set to 40 MPa.

size can be small and the particle size variation is also small. If the melt superheat temperature is not high enough, the melt droplet starts to solidify before the secondary breakup is completed. When the melt temperature becomes lower than the liquidus temperature, its viscosity will increase quickly, which results in the interruption of the further breakup process. Hence, the final particle size will be larger. Due to the large variations in the cooling rates of the droplets with different sizes, locations, and speeds, the interruption of the droplet breakup process due to its solidification can lead to a large variation in the final particle size. Similar trends are revealed in the simulation results shown in Fig. 21.

5. Conclusions

A computational fluid dynamics (CFD) based numerical modeling framework is proposed to simulate the gas atomization process of Nickel-Silicon alloy with a focus on predicting the final particle size distribution. In terms of multiphase flow physics, the gas atomization process is divided into two regions: the primary breakup region near the gas atomization nozzle tip and the secondary breakup region downstream within the gas atomization chamber. The primary breakup of the melt stream by a high-pressured inert gas flow jet is simulated using a VOF two-phase flow model in OpenFOAM. The process of melt stream disintegration, ligament pinching off, and primary droplet formation can be captured through the modeling. The secondary breakup of the melt droplets generated at the primary breakup stage is simulated using an Eulerian-Lagragian discrete phase model (DPM) in Ansys Fluent. The movement, secondary breakup, and cooling of the droplets are tracked using a Lagrangian method. To evaluate the model performance, the

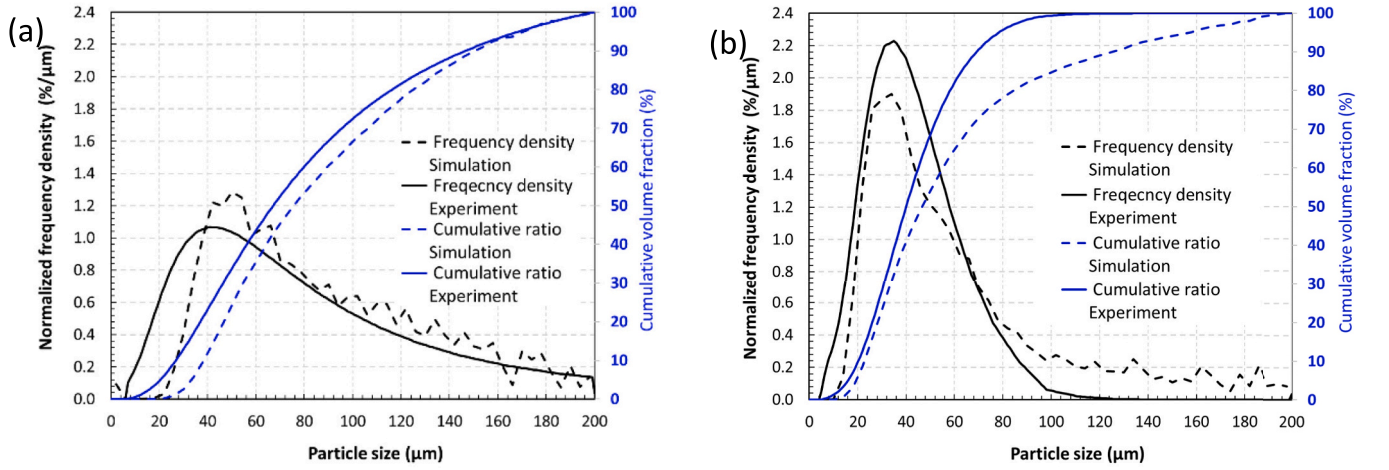

Fig. 15. Comparison of the particle size distribution in the form of normalized frequency density and cumulative volume fraction predicted by the numerical model and those measured in the gas atomization tests. The gas atomization pressures are set to (a) 35 MPa and (b) 45 MPa.

Table 2
Comparison and evaluation of model prediction accuracy of particle size distribution for different gas atomization tests.

Test cases: Gas atomization pressure	Cumulative volume fraction			Frequency density	
	D10 (Sim:Exp)	D50 (Sim:Exp)	D90 (Sim:Exp)	E_{rel}	E_{abs}
Test case A: 35 MPa	38.4: 26.8 μm	75.6: 67.1 μm	150.5: 146.5 μm	19.2%	27%
Test case B: 40 MPa	24.3: 20.6 μm	50.0: 44.7 μm	142.7: 97.5 μm	9.3%	25%
Test case C: 45 MPa	22.8: 20.3 μm	46.6: 40.0 μm	124.7: 60.0 μm	10.1%	38%

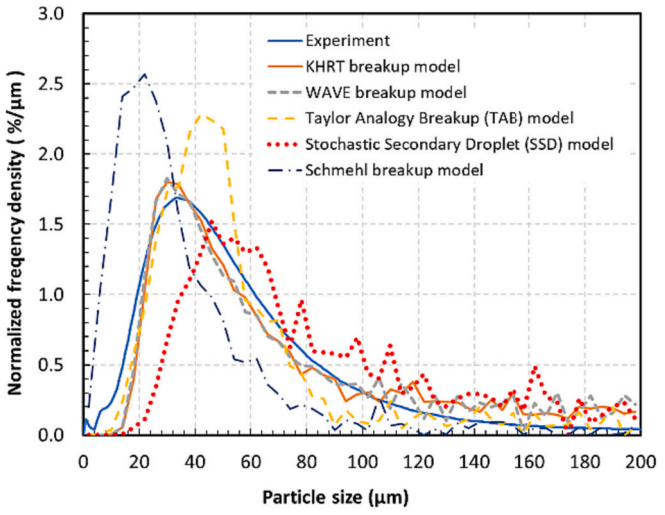

Fig. 16. Particle size distribution predicted by different sub-models for the secondary breakup: Taylor breakup model (TAB); Wave breakup model (Wave); KHRT breakup model (KHRT); Stochastic Secondary Droplet Model (SSD) and Schmehl breakup model.

proposed modeling approach is applied to predict the final particle size distribution obtained from a specially designed gas atomization test of Nickel-Silicon alloy. The model geometry and simulation domain are configured according to the equipment setup (e.g. the gas atomization nozzle and chamber) used in the gas atomization test. The boundary conditions for the modeling (e.g. gas atomization pressure and melt flow rate) are set according to the operating conditions from the gas atomization tests. The material properties (density, specific heat, viscosity, surface tension) of NiSi alloy melt and their variations with temperature are estimated using a software tool – ThermoCalc. The particle size distribution predicted by the proposed modeling approach agrees well with that obtained by the particle size measurement of the powders produced in the gas atomization test.

In addition, various numerical simulations are performed to investigate the effects of different operating parameters (gas pressure, melt flow rate, melt superheat temperature) and melt material properties (viscosity and surface tension) on the particle size distribution. The simulations show how these parameters, when they are decoupled and considered individually, could alter the particle size distribution relatively compared to that obtained in the reference gas atomization test. In general, the condition of higher gas pressure, lower viscosity, lower surface tension, and higher superheat temperature can lead to the formation of finer particles in the gas atomization process. The effect of the

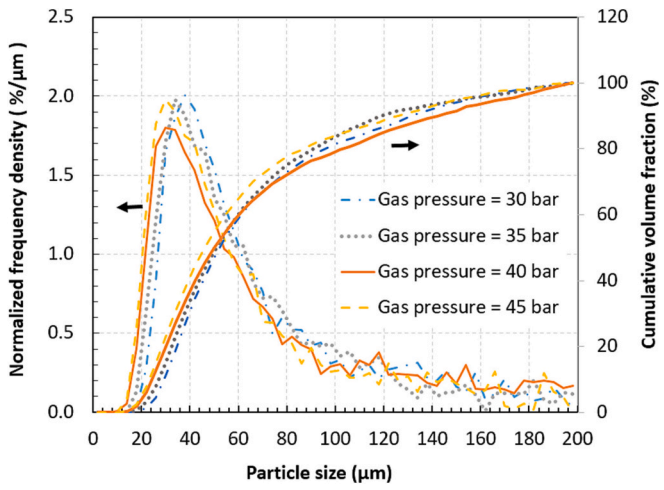

Fig. 17. Particle size distribution after secondary breakup under different inlet gas operating pressures at 30, 35, 40, and 45 bar.

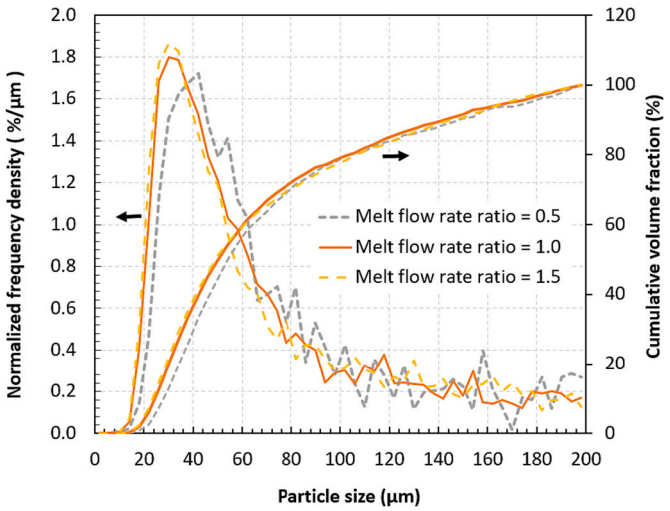

Fig. 18. Particle size distribution after secondary breakup under different inlet flow rate ratios of melt stream: $\frac{\dot{m}_l}{\dot{m}_{l,ref}} = 0.5$, 1.0 and 1.5. $\dot{m}_{l,ref} = 1.26\ kg/min$.

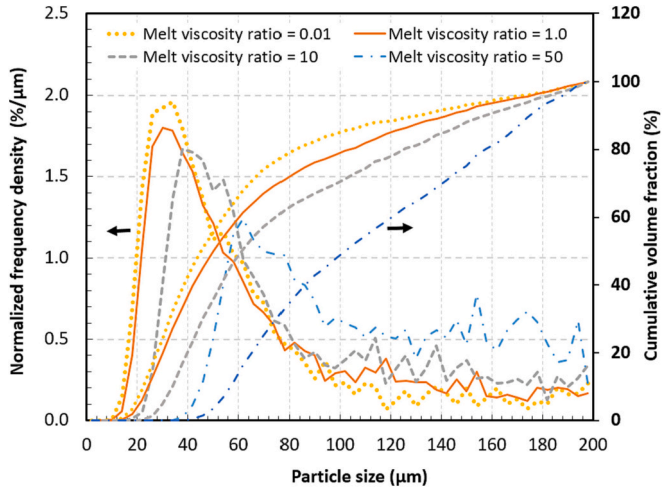

Fig. 19. Particle size distribution under different melt viscosity ratios: $\frac{\nu_l}{\nu_{ref}} = 0.01, 1.0, 10$ *and* 50. $\nu_{ref} = 1.2 \times 10^{-6}\ m^2/s$.

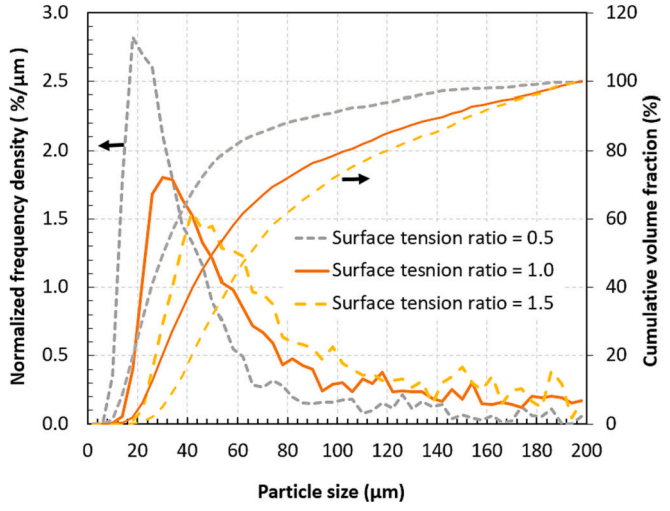

Fig. 20. Particle size distribution under different melt surface tension ratios: $\frac{\sigma}{\sigma_{ref}} = 0.5, 1.0$ *and* 2.0. $\sigma_{ref} = 1.26\ N/m$.

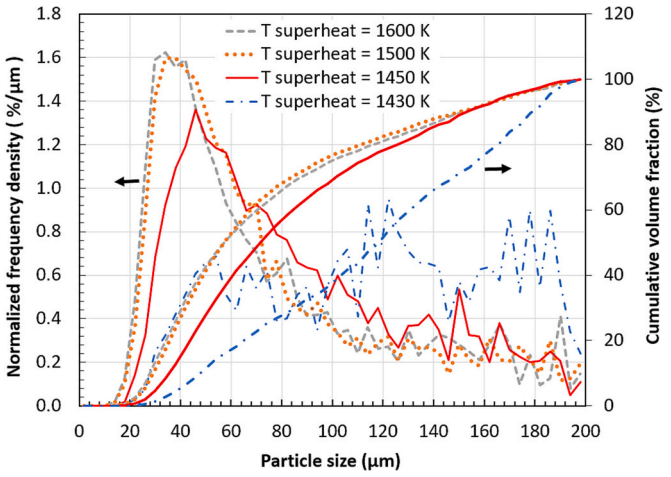

Fig. 21. Comparison of the particle size distribution after secondary breakup under different melt superheat temperatures at 1600 K, 1500 K, 1450 K, and 1430 K.

melt flow rate can be trivial depending on the melt steam flow pattern near the nozzle tip. It should be pointed out that the effects of these operating parameters and material properties are always coupled with each other in reality. It causes challenges in controlling the gas atomization process to get optimized particle size distribution of the produced powders. The numeral modeling approach provides us with an alternative method to investigate the flow physics of the gas atomization process and understand the effects of different operating parameters and material properties. With this knowledge, the gas atomization process can be optimized for different materials and atomization equipment to produce quality powders for different applications.

CRediT authorship contribution statement

Jinsong Hua: Writing – review & editing, Writing – original draft, Validation, Project administration, Methodology, Investigation, Formal analysis, Data curation, Conceptualization. **Federico Simone Gobber:** Writing – review & editing, Writing – original draft, Validation, Investigation, Formal analysis, Data curation. **Marco Actis Grande:** Writing – review & editing, Validation, Supervision, Project administration. **Dag Mortensen:** Writing – review & editing, Resources, Project administration, Methodology, Funding acquisition, Conceptualization. **Jan Ove Odden:** Writing – review & editing, Resources, Project administration, Funding acquisition, Conceptualization.

Declaration of competing interest

The authors declare that they have no known competing financial interests or personal relationships that could have appeared to influence the work reported in this paper.

Data availability

Data will be made available on request.

Acknowledgments

The authors would like to thank the financial support from the Research Council of Norway on the project titled “Development and Production of Metal Alloys for Powder-based Additive Manufacturing (MADAM)” with project no. 309856. Further financial support was given from the Italian Government within the Ministerial Decree no. 1062/2021 which received funding from the FSE REACT-EU - PON Ricerca e Innovazione 2014-2020.

Special thanks should be given to Dr. Even Wilberg Hovig from SINTEF, Norway, for providing us with NiSi alloy material properties using Thermo-Calc.

References

[1] A. Vafadar, F. Guzzomi, A. Rassau, K. Hayward, Advances in metal additive manufacturing: a review of common processes, industrial applications, and current challenges, Appl. Sci. Basel 11 (2021), https://doi.org/10.3390/app11031213.

[2] J.A. Slotwinski, E.J. Garboczi, P.E. Stutzman, C.F. Ferraris, S.S. Watson, M.A. Peltz, Characterization of metal powders used for additive manufacturing, J. Res. Natl. Inst. Stan. 119 (2014) 460–493, https://doi.org/10.6028/jres.119.018.

[3] G. Lewis, Aspects of the powder in metal additive manufacturing: a review, World J. Eng. Technol. 10 (2022) 363–409, https://doi.org/10.4236/wjet.2022.102022.

[4] L.V.M. Antony, R.G. Reddy, Processes for production of high-purity metal powders, Jom-J. Min. Met. Mat. S 55 (2003) 14–18, https://doi.org/10.1007/s11837-003-0153-4.

[5] L.H. Xu, X.L. Zhou, J.H. Li, Y.F. Hu, H. Qi, W. Wen, K.P. Du, Y. Ma, Y.G. Yu, Numerical simulations of molten breakup behaviors of a de Laval-type nozzle, and the effects of atomization parameters on particle size distribution, Processes 8 (2020), https://doi.org/10.3390/pr8091027.

[6] Y.T. Shi, W.Y. Lu, W.H. Sun, S.D. Zhang, B.J. Yang, J.Q. Wang, Impact of gas pressure on particle feature in Fe-based amorphous alloy powders via gas atomization: simulation and experiment, J. Mater. Sci. Technol. 105 (2022) 203–213, https://doi.org/10.1016/j.jmst.2021.06.075.

[7] K.H. Arachchilage, M. Haghshenas, S. Park, L. Zhou, Y. Sohn, B. McWilliams, K. Cho, R. Kumar, Numerical simulation of high-pressure gas atomization of two-phase flow: effect of gas pressure on droplet size distribution, Adv. Powder Technol. 30 (2019) 2726–2732, https://doi.org/10.1016/j.apt.2019.08.019.

[8] E. Urionabarrenetxea, A. Avello, A. Rivas, J.M. Martin, Experimental study of the influence of operational and geometric variables on the powders produced by close-coupled gas atomisation, Mater Design 199 (2021), https://doi.org/10.1016/j.matdes.2020.109441.

[9] X.G. Li, Q. Zhu, S. Shu, J.Z. Fan, S.M. Zhang, Fine spherical powder production during gas atomization of pressurized melts through melt nozzles with a small inner diameter, Powder Technol. 356 (2019) 759–768, https://doi.org/10.1016/j.powtec.2019.09.023.

[10] W.S. Prashanth, S.L. Thotarath, S. Sarkar, T.N.C. Anand, S. Bakshi, Experimental investigation on the effect of melt delivery tube position on liquid metal atomization, Adv. Powder Technol. 32 (2021) 693–701, https://doi.org/10.1016/j.apt.2021.01.017.

[11] P. Wang, J. Li, X. Wang, H.S. Liu, B. Fan, P. Gan, R.F. Guo, X.Y. Ge, M.H. Wang, Close-coupled nozzle atomization integral simulation and powder preparation using vacuum induction gas atomization technology, Chin. Phys. B 30 (2021), https://doi.org/10.1088/1674-1056/abc167.

[12] A. Unal, Liquid break-up in gas atomization of fine aluminum powders, Metall. Trans. B 20 (1989) 61–69, https://doi.org/10.1007/Bf02670350.

[13] S. Luo, Y. Ouyang, Q.L. Wei, S.Y. Lai, Y. Wu, H.W. Wang, H.Z. Wang, Understanding the breakup behaviors of liquid jet in gas atomization for powder production, Mater Design 227 (2023), https://doi.org/10.1016/j.matdes.2023.111793.

[14] E. Urionabarrenetxea, J.M. Martin, A. Avello, A. Rivas, Simulation and validation of the gas flow in close-coupled gas atomisation process: influence of the inlet gas pressure and the throat width of the supersonic gas nozzle, Powder Technol. 407 (2022), https://doi.org/10.1016/j.powtec.2022.117688.

[15] B. Qaddah, P. Chapelle, J.P. Bellot, J. Jourdan, N. Rimbert, A. Deborde, R. Hammes, A. Franceschini, Swirling supersonic gas flow in an EIGA atomizer for metal powder production: numerical investigation and experimental validation, J. Mater. Process. Technol. 311 (2023), https://doi.org/10.1016/j.jmatprotec.2022.117814.

[16] S. Motaman, A.M. Mullis, R.F. Cochrane, D.J. Borman, Numerical and experimental investigations of the effect of melt delivery nozzle design on the open-to closed-wake transition in closed-coupled gas atomization, Metall. Mater. Trans. B Process Metall. Mater. Process. Sci. 46 (2015) 1990–2004, https://doi.org/10.1007/s11663-015-0346-6.

[17] P. Wang, J. Li, H.S. Liu, X. Wang, B.R. Du, P. Gan, S.Y. Shen, B. Fan, X.Y. Ge, M. H. Wang, Process modeling gas atomization of close-coupled ring-hole nozzle for 316L stainless steel powder production, Chin. Phys. B 30 (2021), https://doi.org/10.1088/1674-1056/abd771.

[18] X.G. Li, U. Fritsching, Process modeling pressure-swirl-gas-atomization for metal powder production, J. Mater. Process. Technol. 239 (2017) 1–17, https://doi.org/10.1016/j.jmatprotec.2016.08.009.

[19] J.S. Thompson, O. Hassan, S.A. Rolland, J. Sienz, L.D. Ltd, The identification of an accurate simulation approach to predict the effect of operational parameters on the particle size distribution (PSD) of powders produced by an industrial close-coupled gas atomiser, Powder Technol. 291 (2016) 75–85, https://doi.org/10.1016/j.powtec.2015.12.001.

[20] R. Kaiser, C. Li, S. Yang, D. Lee, A numerical simulation study of the path-resolved breakup behaviors of molten metal in high-pressure gas atomization: with emphasis on the role of shock waves in the gas/molten metal interaction, Adv. Powder Technol. 29 (2018) 623–630, https://doi.org/10.1016/j.apt.2017.12.003.

[21] N. Zeoli, S. Gu, Computational simulation of metal droplet break-up, cooling and solidification during gas atomisation, Comput. Mater. Sci. 43 (2008) 268–278, https://doi.org/10.1016/j.commatsci.2007.10.005.

[22] M.M. Tong, D.J. Browne, Direct numerical simulation of melt-gas hydrodynamic interactions during the early stage of atomisation of liquid intermetallic, J. Mater. Process. Technol. 202 (2008) 419–427, https://doi.org/10.1016/j.jmatprotec.2007.10.012.

[23] N. Zeoli, H. Tabbara, S. Gu, CFD modeling of primary breakup during metal powder atomization, Chem. Eng. Sci. 66 (2011) 6498–6504, https://doi.org/10.1016/j.ces.2011.09.014.

[24] W.J. Zhao, F.Y. Cao, Z.L. Ning, G.G. Zhang, Z. Li, J.F. Sun, A computational fluid dynamics (CFD) investigation of the flow field and the primary atomization of the close coupled atomizer, Comput. Chem. Eng. 40 (2012) 58–66, https://doi.org/10.1016/j.compchemeng.2012.02.014.

[25] P. Wang, X. Zhou, X. Li, Z. Chen, Q. Hu, X. Wang, Z. Yu, Numerical and experimental investigation of close-coupled twin-nozzle gas atomization towards fine high-entropy alloy powder production, J. Mater. Process. Technol. 324 (2024), https://doi.org/10.1016/j.jmatprotec.2023.118238.

[26] D.A. Firmansyah, R. Kaiser, R. Zahaf, Z. Coker, T.Y. Choi, D. Lee, Numerical simulations of supersonic gas atomization of liquid metal droplets, Jpn. J. Appl. Phys. 53 (2014), https://doi.org/10.7567/Jjap.53.05ha09.

[27] M.W. Wei, S.Y. Chen, M. Sun, J. Liang, C.S. Liu, M. Wang, Atomization simulation and preparation of 24CrNiMoY alloy steel powder using VIGA technology at high gas pressure, Powder Technol. 367 (2020) 724–739, https://doi.org/10.1016/j.powtec.2020.04.030.

[28] S. Luo, H.Z. Wang, Z.Y. Gao, Y. Wu, H.W. Wang, Interaction between high-velocity gas and liquid in gas atomization revealed by a new coupled simulation model, Mater Design 212 (2021), https://doi.org/10.1016/j.matdes.2021.110264.

[29] P. Wang, J.Q. Liu, Y.N. Dong, Z.Q. Zhu, J. Pang, J.Q. Zhang, Breakup process modeling and production of FeSiAl magnetic powders by close-coupled gas atomization, J. Mater. Res. Technol. 23 (2023) 730–743, https://doi.org/10.1016/j.jmrt.2022.12.169.

[30] A. Amatriain, E. Urionabarrenetxea, A. Avello, J.M. Martín, Multiphase model to predict particle size distributions in close-coupled gas atomization, Int. J. Multiphase Flow 154 (2022) 104138, https://doi.org/10.1016/j.ijmultiphaseflow.2022.104138.

[31] J.U. Brackbill, D.B. Kothe, C. Zemach, A continuum method for modeling surface-tension, J. Comput. Phys. 100 (1992) 335–354, https://doi.org/10.1016/0021-9991(92)90240-Y.

[32] V.A. Vuorinen, H. Hillamo, O. Kaario, M. Nuutinen, M. Larmi, L. Fuchs, Effect of droplet size and atomization on spray formation: a priori study using large-Eddy simulation, Flow Turbul. Combust. 86 (2011) 533–561, https://doi.org/10.1007/s10494-010-9266-3.

[33] G.I. Taylor, The shape and acceleration of a drop in a high speed air stream, in: G. K. Batchelor (Ed.), The Scientific Papers of sir Geoffrey Ingram Taylor: Volume 3, Aerodynamics and the Mechanics of Projectiles and Explosions, Cambridge University Press, 1963.

[34] R.D. Reitz, Mechanisms of atomization processes in high-pressure vaporizing sprays, Atomiz. Spray Technol. 3 (1987) 309–337.

[35] M.R. Turner, S.S. Sazhin, J.J. Healey, C. Crua, S.B. Martynov, A breakup model for transient Diesel fuel sprays, Fuel 97 (2012) 288–305, https://doi.org/10.1016/j.fuel.2012.01.076.

[36] J.C. Beale, R.D. Reitz, Modeling spray atomization with the Kelvin-Helmholtz/Rayleigh-Taylor hybrid model, Atomiz. Spray 9 (1999) 623–650.

[37] D.D. Joseph, J. Belanger, G.S. Beavers, Breakup of a liquid drop suddenly exposed to a high-speed airstream, Int. J. Multiphase Flow 25 (1999) 1263–1303, https://doi.org/10.1016/S0301-9322(99)00043-9.

[38] R. Schmehl, G. Klose, G. Maier, S. Wittig, Efficient numerical calculation of evaporating sprays in combustion chamber flows, in: RTO AVTSymposium on Gas Turbine Engine Combustion Emissions and Alternative Fuels, Lisbon, Portugal, 1998. RTO MP-14, pp. 51.51–51.14.

[39] S.V. Apte, M. Gorokhovski, P. Moin, LES of atomizing spray with stochastic modeling of secondary breakup, Int. J. Multiphase Flow 29 (2003) 1503–1522, https://doi.org/10.1016/S0301-9322(03)00111-3.

[40] C. Daskiran, L. R, K. Lee, J. Katz, M.C. Boufadel, Estimation of overall droplet size distribution from a local droplet size distribution for a jet in crossflow: experiment and multiphase large eddy simulations, Int. J. Multiphase Flow 156 (2022), https://doi.org/10.1016/j.ijmultiphaseflow.2022.104205.

[41] F. Salehi, M. Ghiji, L.F. Chen, Large eddy simulation of high pressure spray with the focus on injection pressure, Int. J. Heat Fluid Fl 82 (2020), https://doi.org/10.1016/j.ijheatfluidflow.2020.108551.

[42] S.B. Pope, Turbulent Flows, Cambridge University Press, Cambridge, 2001.

[43] F.F. Grinstein, L.G. Margolin, W.J. Rider, Implicit Large Eddy Simulation, Cambridge University Press, Cambridge, 2007.

[44] L. Battezzati, A.L. Greer, The viscosity of liquid metals and alloys, Acta Metall. 37 (1989) 1791–1802, https://doi.org/10.1016/0001-6160(89)90064-3.

[45] J.S. Hua, B.L. Zhang, J. Lou, Numerical simulation of microdroplet formation in coflowing immiscible liquids, AICHE J. 53 (2007) 2534–2548, https://doi.org/10.1002/aic.11287.